Article

Cell Reports

Lymphatic network drainage resolves cerebral edema and facilitates recovery from experimental cerebral malaria

Graphical abstract

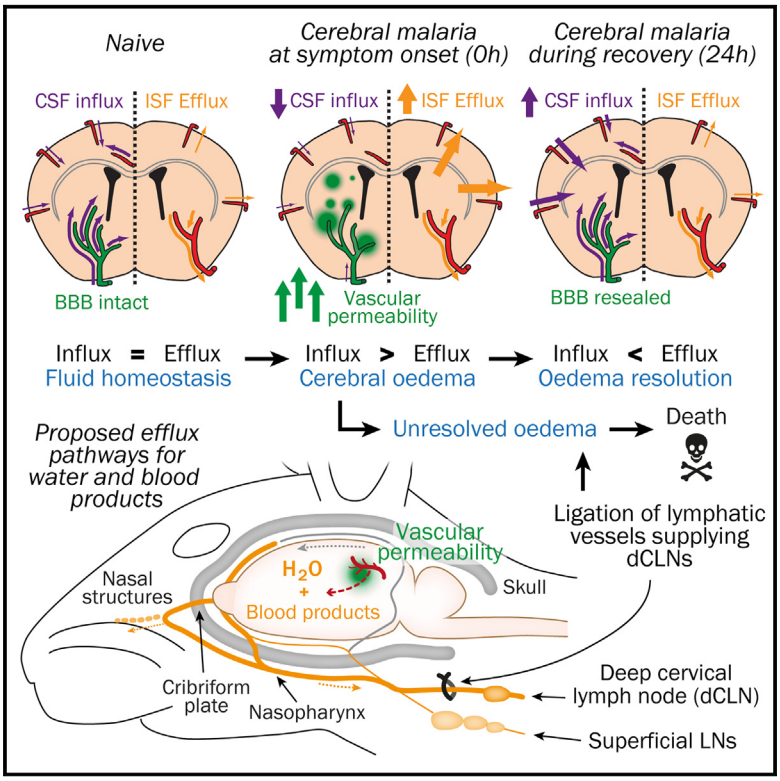

Highlights

- Vasogenic edema is a pathological feature of experimental cerebral malaria (ECM)
- Basal meningeal and nasal lymphatic networks clear edematous fluid during ECM
- Ligation of deep cervical lymph nodes inhibits edematous fluid removal during ECM

Authors

Michael J. Haley, Ruben Barroso, Dhifaf A. Jasim, ..., Alister G. Craig, David Brough, Kevin N. Couper

Correspondence

kevin.couper@manchester.ac.uk

In brief

Haley et al. show that recovery from experimental cerebral malaria (ECM) is dependent on the rapid drainage of fluid from the skull through lymphatic vessels within the base of the brain and the nasal regions, connecting to the deep cervical lymph nodes.

Haley et al., 2024, Cell Reports *43*, 114217
May 28, 2024
https://doi.org/10.1016/j.celrep.2024.114217

CellPress

Cell Reports

CellPress
OPEN ACCESS

Article

Lymphatic network drainage resolves cerebral edema and facilitates recovery from experimental cerebral malaria

Michael J. Haley,[1,2,3] Ruben Barroso,[1,2,3] Dhifaf A. Jasim,[4,5] Megan Haigh,[1] Jack Green,[2,3,8] Ben Dickie,[2,6] Alister G. Craig,[7] David Brough,[2,3,8] and Kevin N. Couper[1,2,3,9,*]

[1]Division of Immunology, Immunity to Infection & Respiratory Medicine, Faculty of Biology, Medicine & Health, The University of Manchester, Manchester M13 9PT, UK

[2]Geoffrey Jefferson Brain Research Centre, The Manchester Academic Health Science Centre, Northern Care Alliance NHS Group, University of Manchester, Manchester, UK

[3]The Lydia Becker Institute of Immunology and Inflammation, University of Manchester, Manchester, UK

[4]Nanomedicine Lab, National Graphene Institute and Faculty of Biology, Medicine & Health, The University of Manchester, AV Hill Building, Manchester M13 9PT, UK

[5]Medicines Discovery Catapult (MDC), Alderley Park, Macclesfield SK10 4TG, UK

[6]Division of Informatics, Imaging & Data Sciences, Faculty of Biology, Medicine & Health, The University of Manchester, Manchester M13 9PT, UK

[7]Department of Tropical Disease Biology, Liverpool School of Tropical Medicine, Liverpool L3 5QA, UK

[8]Division of Neuroscience, Faculty of Biology, Medicine & Health, The University of Manchester, Manchester M13 9PT, UK

[9]Lead contact

*Correspondence: kevin.couper@manchester.ac.uk

https://doi.org/10.1016/j.celrep.2024.114217

SUMMARY

While brain swelling, associated with fluid accumulation, is a known feature of pediatric cerebral malaria (CM), how fluid and macromolecules are drained from the brain during recovery from CM is unknown. Using the experimental CM (ECM) model, we show that fluid accumulation in the brain during CM is driven by vasogenic edema and not by perivascular cerebrospinal fluid (CSF) influx. We identify that fluid and molecules are removed from the brain extremely quickly in mice with ECM to the deep cervical lymph nodes (dcLNs), predominantly through basal routes and across the cribriform plate and the nasal lymphatics. In agreement, we demonstrate that ligation of the afferent lymphatic vessels draining to the dcLNs significantly impairs fluid drainage from the brain and lowers anti-malarial drug recovery from the ECM syndrome. Collectively, our results provide insight into the pathways that coordinate recovery from CM.

INTRODUCTION

Cerebral malaria (CM) is a severe complication of *Plasmodium falciparum* infection that affects primarily young children in Sub-Saharan Africa. Currently, there are no specific treatments for CM, other than parenteral administration of anti-malarial drugs (principally artemisinin). This treatment fails to prevent death in 15%–20% of cases, equating to 300–400 thousand deaths each year.[1] Children who survive the syndrome also frequently exhibit severe neurological disorders that can be long-lasting, including ataxia, speech disorders, cortical blindness, cognitive impairment, and epilepsy.[2–4]

While the pathogenesis of pediatric CM is still incompletely understood, fulminant brain swelling has been identified as a primary cause of morbidity and mortality.[5–9] The cause of brain swelling during CM has been debated with sequestration of parasitized cells within the cerebrovasculature, increased blood flow and loss of autoregulation, cytotoxic edema, and vasogenic edema all being implicated.[5,8] However, extensive vasogenic edema has been identified within the brains of children with pediatric CM.[8–10] This corresponds with evidence of blood-brain barrier (BBB) dysfunction (generally in vessels associated with parasitized red blood cell sequestration or thrombosis) within a number of brain regions.[10–14] Notably, damage to the BBB and vasogenic edema has also been implicated in causing the secondary parenchymal pathologies observed in pediatric CM, including axonal injury, myelin damage, and neuroinflammation (astrocyte and macrophage activation).[11,13] In children who survive CM, brain swelling is transient and rapidly reversible within a few days.[5,10,14,15] The rapid drainage of vasogenic edema fluid and amelioration of brain swelling suggests that highly effective physiological systems operate within the CNS to coordinate recovery from CM.

How fluid and macromolecules drain from the cranium is an area of intense research relevant for understanding homeostatic regulation of interstitial fluid (ISF) volume, clearance of metabolic waste and damaging materials, and immune surveillance of the CNS (reviewed by Rasmussen et al. and others[16–20]). Various

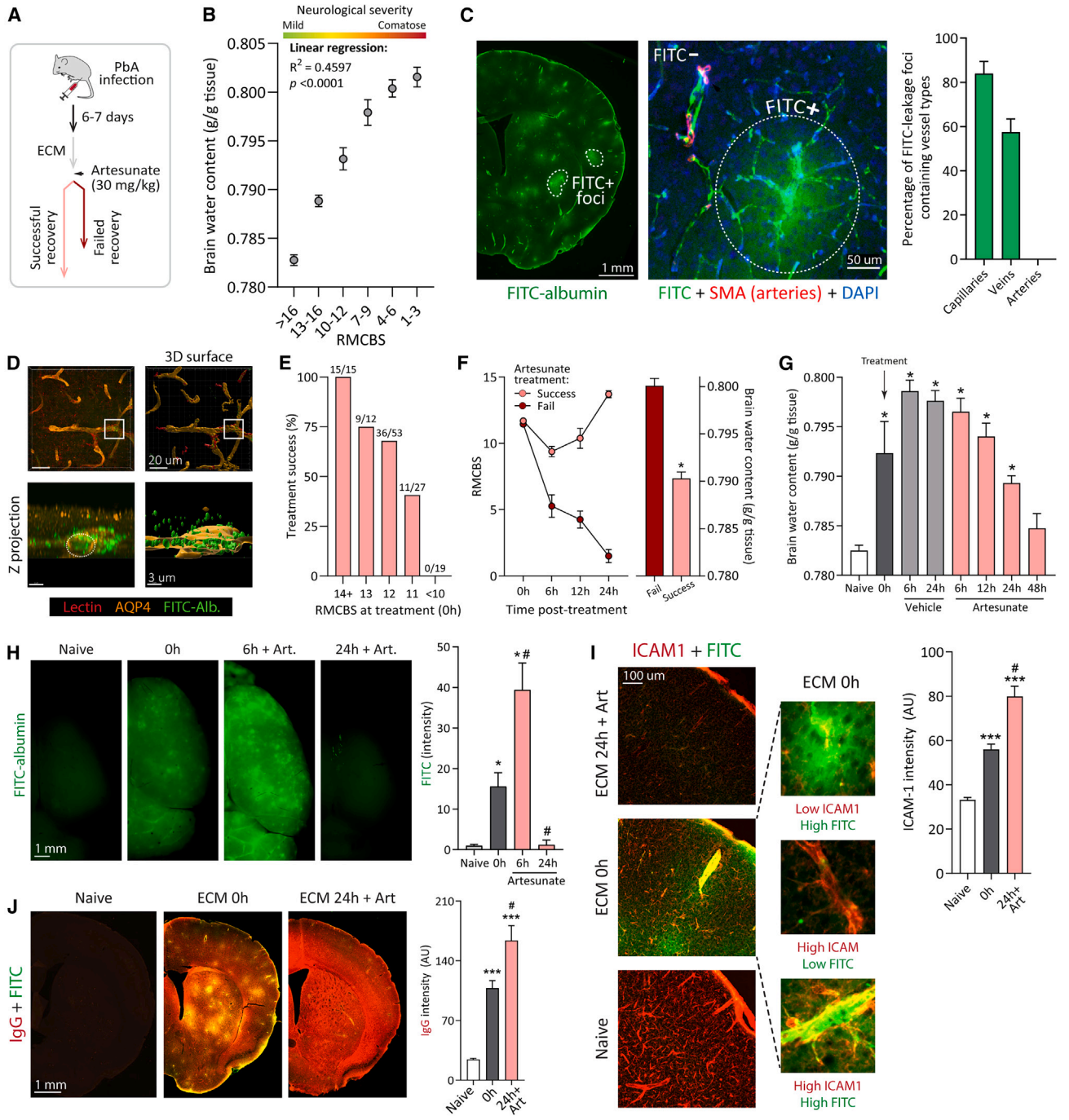

Figure 1. The kinetics of fluid accumulation and clearance in the brain during ECM and following anti-malarial drug treatment

(A) Schematic outlining the experimental design to examine anti-malarial drug treatment of established ECM. Brains were removed from mice at different time points following *P. berghei* ANKA infection and anti-malarial drug (artesunate) treatment.

(B) The brain water content in mice with different severities of ECM, defined by the RMCBS scale (with a score of 11–12 representing established ECM and <7 late stage ECM), n = 192.

(C) Representative images and calculated proportional leakage of i.v. FITC-albumin in cerebral vessel types during ECM, n = 14.

(D) Reconstructed images showing FITC-albumin leakage across vessel barriers during ECM.

(E) The percentage recovery of mice administered artesunate at different stages of ECM, n = 126 total.

(F) The level of brain water content in mice that survived or failed artesunate treatment of ECM. Student's t test, n = 44–57, $^*p < 0.0001$.

(G) Time course of brain water content in mice following artesunate treatment (or vehicle control) of established ECM. One-way ANOVA with Dunnett's post hoc, n = 4–22, total 79 animals, $^*p < 0.0001$ vs. naive.

(legend continued on next page)

different routes for ISF and macromolecule efflux from the cranium have been proposed, including drainage through dorsal and basal lymphatic networks within the meninges.[21–25] Cerebrospinal fluid (CSF) and ISF have also been shown to drain from the skull by crossing the cribriform plate and egressing via lymphatic networks within the nasal mucosa.[26–28] The linkage between the nasal and meningeal lymphatic networks has been debated,[29] but they appear to connect through the nasopharyngeal plexus for draining to the cervical lymph nodes.[30]

At present, the relative importance of the meningeal and nasal CNS lymphatic networks for removal of vasogenic edema, amelioration of brain swelling, and recovery from CM is unknown. To address this, we have utilized the tractable murine model of experimental cerebral malaria (ECM). We, and others, have previously analyzed the ECM model for assessing the pathways controlling the recovery from CM following anti-malarial drug treatment.[6,31–36] Here, we show that, in mice with ECM and following anti-malarial drug treatment, fluid and macromolecules are rapidly removed from the brain parenchyma and are transported, predominantly through basal and nasal routes, to the deep cervical lymph nodes (dcLNs). Ligation of dcLNs restricted fluid removal, exacerbated brain swelling, and undermined recovery from ECM. Our results provide insight into the clearance systems employed to support recovery from CM and help prioritize design of treatments for the syndrome.

RESULTS

The dynamics of water accumulation and removal from the brain following anti-malarial drug treatment of ECM

To study the physiologic systems that coordinate fluid removal during recovery from CM, we first validated the murine ECM-anti-malarial drug cure model (Figure 1A). We confirmed that ECM was associated with a significant increase in brain water accumulation and that the severity of ECM, as defined by RMCBS grading, was directly correlated with the level of brain water (Figure 1B). Water accumulation during agonal ECM was associated with vasogenic edema emanating from damage to the BBB within smooth muscle actin-negative (SMA^-) capillaries and veins, but not SMA^+ arteries (Figure 1C). Intravascular tracers leaking from the damaged BBB accumulated within perivascular spaces (PVSs) and crossed the glial limitans (defined by AQP4 staining) into the brain parenchyma (Figure 1D). Histologically, edema during ECM was visible in H&E-stained sections in the white matter and as perivascular cuffing (Figure S1). Crucially, we also identified that anti-malarial drug (artesunate) treatment success of ECM was governed by the severity of the syndrome (as defined by RMCBS score and, by proxy, the level of fluid accumulation) at time point of treatment, as well as the capacity to regulate brain water content post-administration (Figures 1E and 1F). These data indicate that intracerebral fluid accumulation is a key pathological feature of ECM, controlling the severity of the syndrome as well as treatment effectiveness, equivalent to observations in pediatric CM.

We subsequently assessed the dynamics of edematous fluid accumulation and removal from the brain following anti-malarial drug treatment of ECM (mice treated at RMCBS 11–12; survival at this stage of ECM development varied slightly from 40% to 60%, depending on the infection). Fluid accumulation in the brain continued to increase in the immediate period after anti-malarial drug administration, peaking at 6–12 h post-treatment, before returning rapidly to normal levels by 48 h post-administration (Figure 1G). Notably, anti-malarial drug administration failed to mitigate fluid increase compared with vehicle administration in the acute 6-h period post-treatment (Figure 1G). In agreement, anti-malarial drugs failed to substantially repair the BBB within the first 6 h of treatment (as shown by leakage of vascular FITC-albumin tracer, injected 30 min prior to termination) (Figure 1H), potentially providing a mechanistic reason for the continued mortality seen directly after anti-malarial drug treatment of CM. The BBB was, however, fully resealed at 24 h after anti-malarial drug treatment, emphasizing global and uniform BBB repair (Figure 1H). At the time point of anti-malarial drug treatment, we observed leakage from vessels expressing high levels of ICAM-1 (a canonical marker of vascular activation and inflammation) but also from vessels with low levels or no ICAM-1 (Figure 1I). We also saw little evidence of leakage in numerous vessels expressing high levels of ICAM-1 (Figure 1I). In addition, vascular ICAM-1 expression was significantly increased at 24 h post-treatment, when the BBB was completely resealed, compared with vessels at the time point of treatment (when BBB leakage was high) (Figure 1I). Thus, opening and subsequent resealing of the BBB during ECM appeared independent of ICAM-1 expression, and potentially endothelial inflammation or activation.

To directly analyze how blood-derived macromolecules enter and subsequently spread within the brain following development of edema during ECM, we examined the distribution of IgG (as a representative blood-derived protein) within the brain parenchyma. IgG was colocalized with vascular FITC-albumin tracer and was focally deposited around areas of BBB damage at the time point of anti-malarial drug treatment (Figure 1J). In contrast, IgG was spread widely throughout the brain parenchyma at 24 h after anti-malarial drug treatment (Figure 1J). Thus, edematous fluid and blood-derived molecules rapidly spread, even after repair of the BBB, throughout the brain parenchyma in the acute time period after anti-malarial drug treatment.

Collectively, these data show the importance and the dynamics of fluid accumulation and drainage in the brain following anti-malarial drug treatment of ECM.

(H) Representative images and calculated level of vascular leakage (measuring i.v. FITC-albumin injected 30 min prior to perfusion and analysis) in brains of mice at 6 and 24 h after anti-malarial drug treatment of established ECM (0 h time point).
(I) Representative images showing vascular leakage (i.v. FITC-albumin) in cerebral vessels with and without signs of inflammation (ICAM-1 expression) during ECM and calculated ICAM-1 expression in the brain following anti-malarial drug treatment of ECM.
(J) The localization and calculated level of IgG within the brain parenchyma in comparison with i.v. FITC-albumin in mice following anti-malarial drug treatment of ECM. Statistics for (H)–(J) all one-way ANOVA with Tukey's post hoc, $n = 7–14$, $^*p < 0.05$, $^{***}p < 0.0001$ vs. naive, $\#p < 0.05$ vs. 0 h. Data are presented as mean ± standard error of mean.

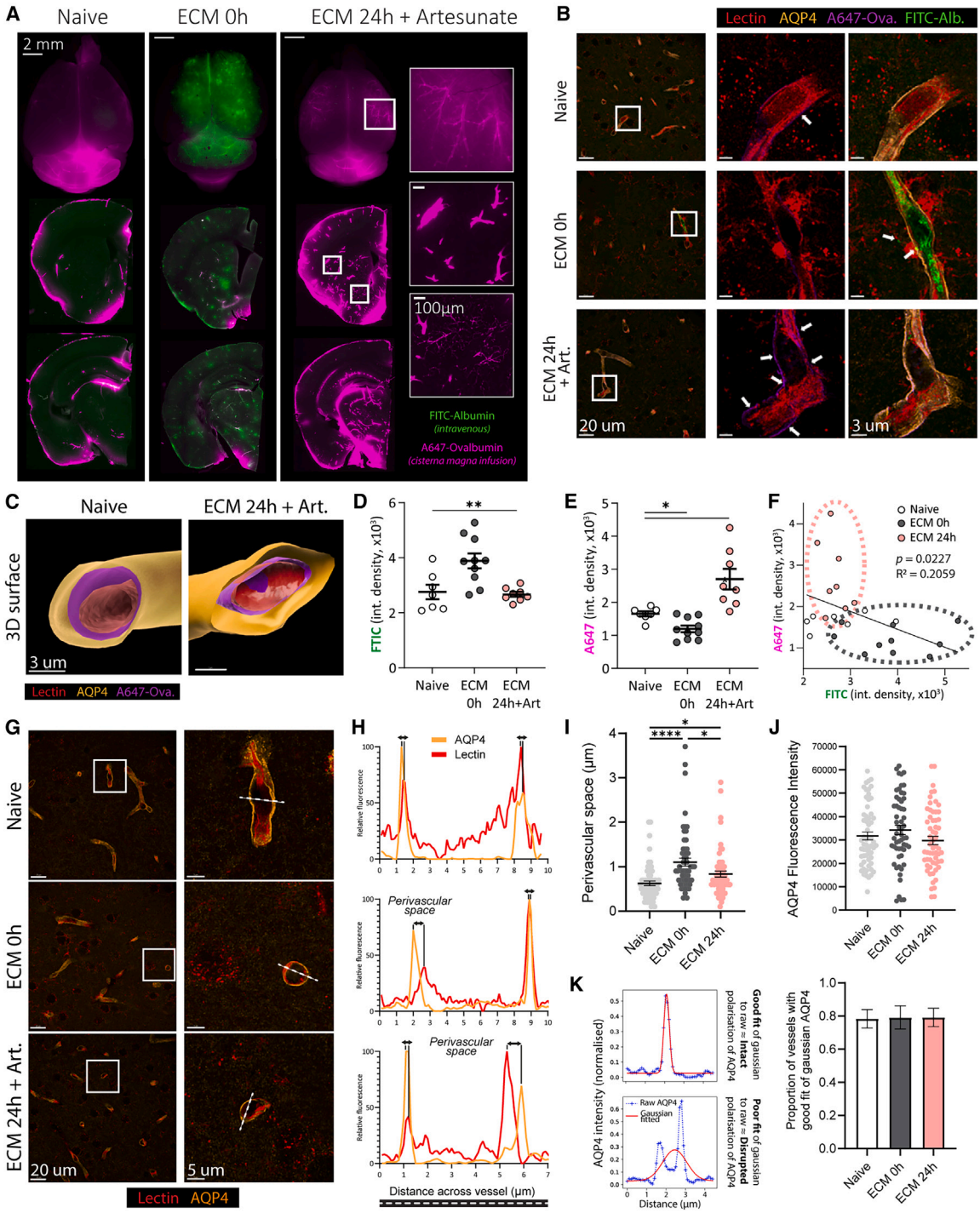

Figure 2. Temporal perturbations in CSF flow in mice with ECM and during recovery from the syndrome

(A) Representative images showing location and level of fluorescent tracers within the brain 30 min following injection into CSF (intra cisterna magna [i.c.m.] A647-ovalbumin, under ketamine/xylazine anesthesia) or blood (i.v. FITC-albumin) in naive mice, mice with ECM (RMCBS 11–12) and mice 18–24 h after treatment with artesunate.

(B and C) (B) Representative images and (C) 3D vessel reconstruction showing perivascular location of CSF tracer (A647-ovalbumin) in comparison with vascular leakage (FITC-albumin) in naive mice, mice with ECM, and in mice during recovery from ECM.

(D–F) Mean intensity levels of (D) blood (FITC), and (E) CSF (A647) tracers in brains of mice, and (F) inverse association of CSF (A647) perfusion into brain compared with vascular leakage (FITC). One-way ANOVA with Dunnett's post hoc, n = 6–10.

(legend continued on next page)

Perivascular CSF influx pathways are temporally altered but do not contribute to edema during ECM following anti-malarial drug treatment

While our data indicated that intracerebral fluid accumulation during ECM was most likely due to damage to the BBB and leakage of fluid from the blood (Figure 1), increased CSF influx into the brain has been shown to contribute to brain edema following stroke and potentially other conditions.[37] Thus, we examined the dynamics of CSF influx, and how this correlated with edematous fluid accumulation and subsequent removal in mice with ECM and following anti-malarial drug treatment, respectively. Active BBB leakage was examined through i.v. injection of FITC-albumin and CSF flow was assessed through injection of A647-ovalbumin into the cisterna magna. CSF tracers injected into the cisterna magna of naive mice showed characteristic distribution throughout the sub-arachnoid space (SAS) and were associated with penetrating cortical vessels (Figure 2A). In contrast, intracisternal tracers injected into mice with ECM failed to circulate in the SAS and appeared to be excluded from the brain (Figure 2A). Circulation and penetration of intracisternal A647-ovalbumin tracer into the brain was, however, elevated in mice at 18–24 h after anti-malarial drug treatment of ECM (Figure 2A). As a control, the dynamics of intracisternal A647-ovalbumin tracer movement was not altered in uninfected mice given anti-malarial drugs (Figure S2A). Notably, intracisternal tracers appeared to accumulate predominantly in PVSs surrounding blood vessels in naive mice and in mice following anti-malarial drug treatment of ECM, including in large penetrating SMA^+ arteries, consistent with the postulated route of CSF influx within the glymphatic pathway (Figures 2B, 2C, and S2B). Mirroring the dynamics of CSF influx, cerebral blood flow was significantly decreased at the time point of anti-malarial drug treatment and was upregulated at 18–24 h post-treatment (Figure S2C).

In agreement with data shown in Figure 1, brain-wide damage to the BBB was evident in mice with ECM (as shown by leakage of intravascular FITC-albumin tracer), whereas the BBB was completely resealed (as shown by lack of intravascular tracer leakage into the brain) at 18–24 h after anti-malarial drug treatment (Figures 2A and 2D). Thus, overall, there was an inverse relationship between CSF perivascular influx and BBB leakage in mice with ECM and following anti-malarial drug treatment (Figures 2E and 2F).

The rate of CSF influx to the brain has been linked to the size of PVSs surrounding cerebral blood vessels and the expression and polarization of the water channel AQP4 at the border of the PVS.[37,38] Indeed, vasoconstriction and enlargement of PVSs is the cause of aberrant CSF flow after stroke.[37] Increased and altered AQP4 expression has also been reported in mice with ECM and following vasogenic edema in other models.[39,40] AQP4 is important for removal of vasogenic edema in conditions associated with BBB damage (reviewed by Papadopoulos and Verkman[41]). Consequently, we examined if PVS and AQP4 levels were altered in mice with ECM and following anti-malarial drug treatment, potentially affecting clearance of vasogenic edema fluid or CSF influx into the brain, respectively. Interestingly, the diameter of capillary PVSs (calculated by measuring mean distance between endothelial cells and AQP4) was significantly increased in mice with ECM, before reducing slightly (but to a level still above baseline in naive mice) at 18–24 h after anti-malarial drug treatment (Figures 2G–2I). In agreement, the sizes of PVSs were significantly increased in mice with ECM and in mice 18–24 h post-treatment, as measured histologically within H&E-stained sections (Figures S3A and S3B). Consequently, dynamic alterations in PVS size may potentially influence CSF movement during recovery from ECM but this does not explain collapse in CSF flow during the established syndrome. There were no differences in either the expression level or polarization of AQP4 in mice with ECM or following anti-malarial drug treatment (Figures 2J, 2K, and S3C).

Combined, these data indicate that perivascular CSF influx is disrupted during ECM, and that CSF influx is unlikely to contribute to fluid accumulation during the syndrome. Conversely, CSF flow is rapidly upregulated during recovery and may coordinate recovery of brain homeostasis. Alterations in AQP4 are also unlikely to contribute to altered fluid dynamics in the brain during ECM and following anti-malarial drug treatment.

Fluid drainage pathways in the brain are highly effective in mice with ECM and during recovery from the syndrome

Raised intracranial pressure (ICP), as is observed in CM,[6,42,43] has been associated with defective fluid clearance from the CNS in other conditions.[44,45] Consequently, to address whether the rapid increase in brain water during ECM corresponded with co-disruption of fluid drainage systems, we injected small (758 Da A594-hydrazide) and large (45 kDa A647-ovalbumin) tracers, to model movement and clearance of fluid and macromolecules, respectively, into the brain striatum in naive mice, mice with ECM immediately prior to anti-malarial drug treatment and into mice at 24 h post-drug treatment (Figure 3A). Intracerebral injections into mice with ECM did not affect the recovery from the syndrome following anti-malarial drug treatment, or the ability to regulate brain water content (Figures S4A–S4C). Injections did not hit ventricles and there was no evidence of reflux of tracers along the needle track, including in mice with ECM (Figure S4D). Artesunate treatment of naive mice did not alter the dynamics of tracer removal from the brain (Figure S4E). At 1 h after injection, both small and large tracers were clearly observed within top and bottom regions of the brain when viewed by stereotaxic microscopy and surrounding the injection site (Figures 3A and 3B). The absolute level (fluorescence intensity) of both tracers trended lower surrounding the injection site and in the top regions of the brain and were significantly lower in the bottom regions of

(G–I) (G) Representative images and (H) histograms showing distance between endothelial lining of vessels (defined by lectin) and astrocyte endfeet (defined by AQP4), with (I) calculated diameter of perivascular space in brains of naive mice, mice with ECM, and in mice 18–24 h after anti-malarial drug treatment.
(J) Mean expression of AQP4 associated with vessels.
(K) Histograms showing modeled intact and disorganized polarization of AQP4 on astrocyte endfeet and calculated proportion of vessels in brains of the different groups of mice with polarized AQP4 expression. Statistics for (I)–(K) all Kruskal-Wallis test with Dunnett's post hoc, 15 cortical vessels analyzed per animal, n = 4/group. (D–F, I) $^*p < 0.05$, $^{**}p < 0.01$, $^{***}p < 0.001$, $^{****}<0.0001$. Data are presented throughout as mean ± standard error of mean.

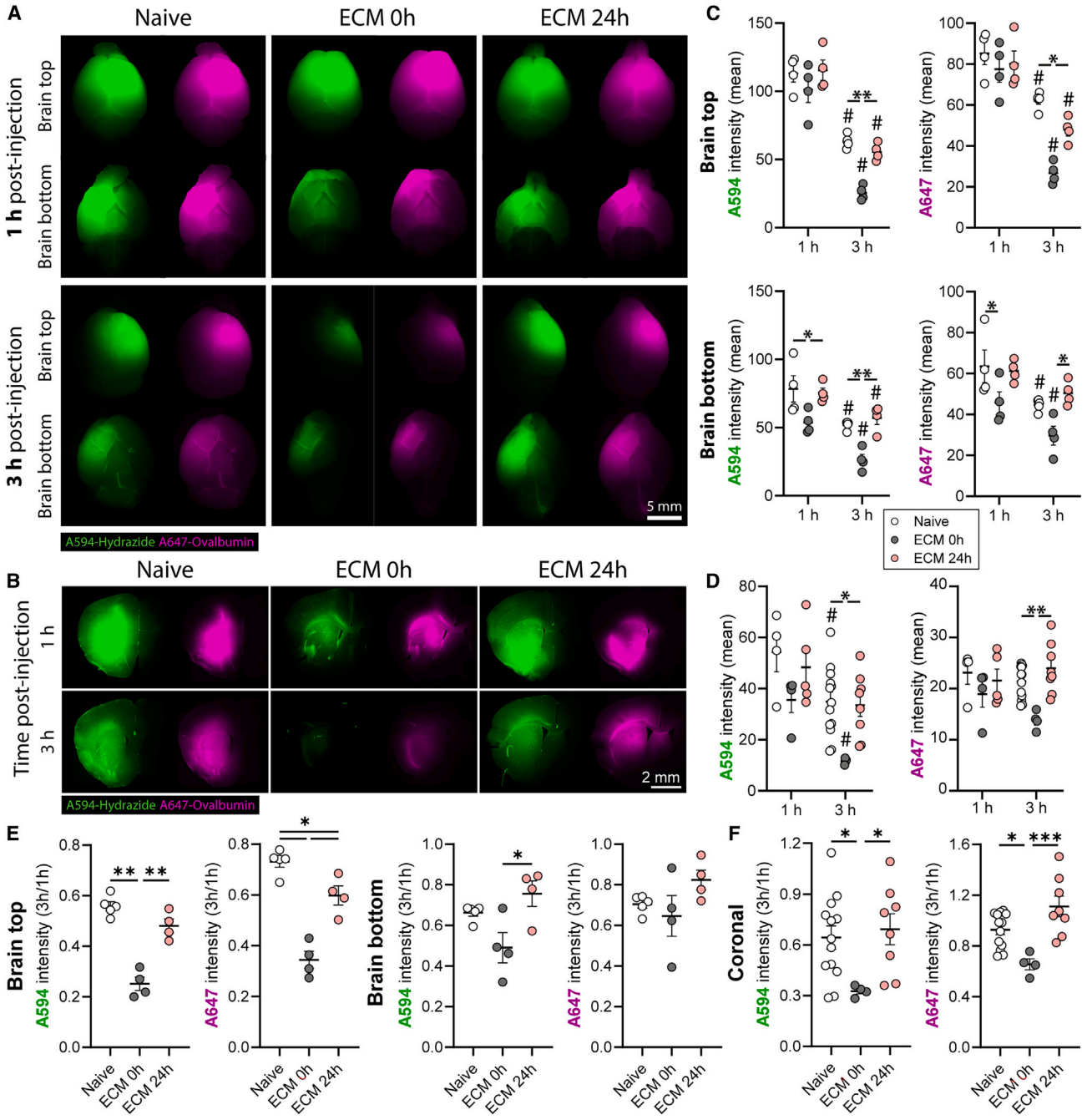

Figure 3. Tracer efflux from the brain is rapid in mice with ECM

Small (Alexa 594-hydrazide) and large (Alexa 647-ovalbumin) tracers were injected together into the brain striatum under isoflurane and recovery anesthesia. (A and B) Representative (A) stereotaxic microscope images of the top and bottom of brain and (B) images surrounding the injection site showing A494 and A647 positions within the brain parenchyma of naive mice, mice with ECM, and in mice 18–24 h following anti-malarial drug treatment at 1 and 3 h post-injection. (C) Quantitation of fluorescence intensity of the tracers in the top and bottom regions of brain, $n = 4–5$.

(D) Quantitation of fluorescence intensity of the tracers in the brain sections surrounding the injection site, $n = 4–13$.

(E and F) The calculated ratio of fluorescence intensity in the brain regions at 3 h post-injection compared with the average intensity at 1 h for each group for (E) stereomicroscopy images of the top and bottom of the brain and (F) coronal sections of the injection site. Statistics were two-way (C and D) or one-way (E and F) ANOVA with Tukey's post hoc, $^{*}p < 0.05$, $^{**}p < 0.01$, $^{***}p < 0.001$, $\#p < 0.05$ compared with equivalent group at 1 h post-injection. Data are presented as mean ± standard error of mean.

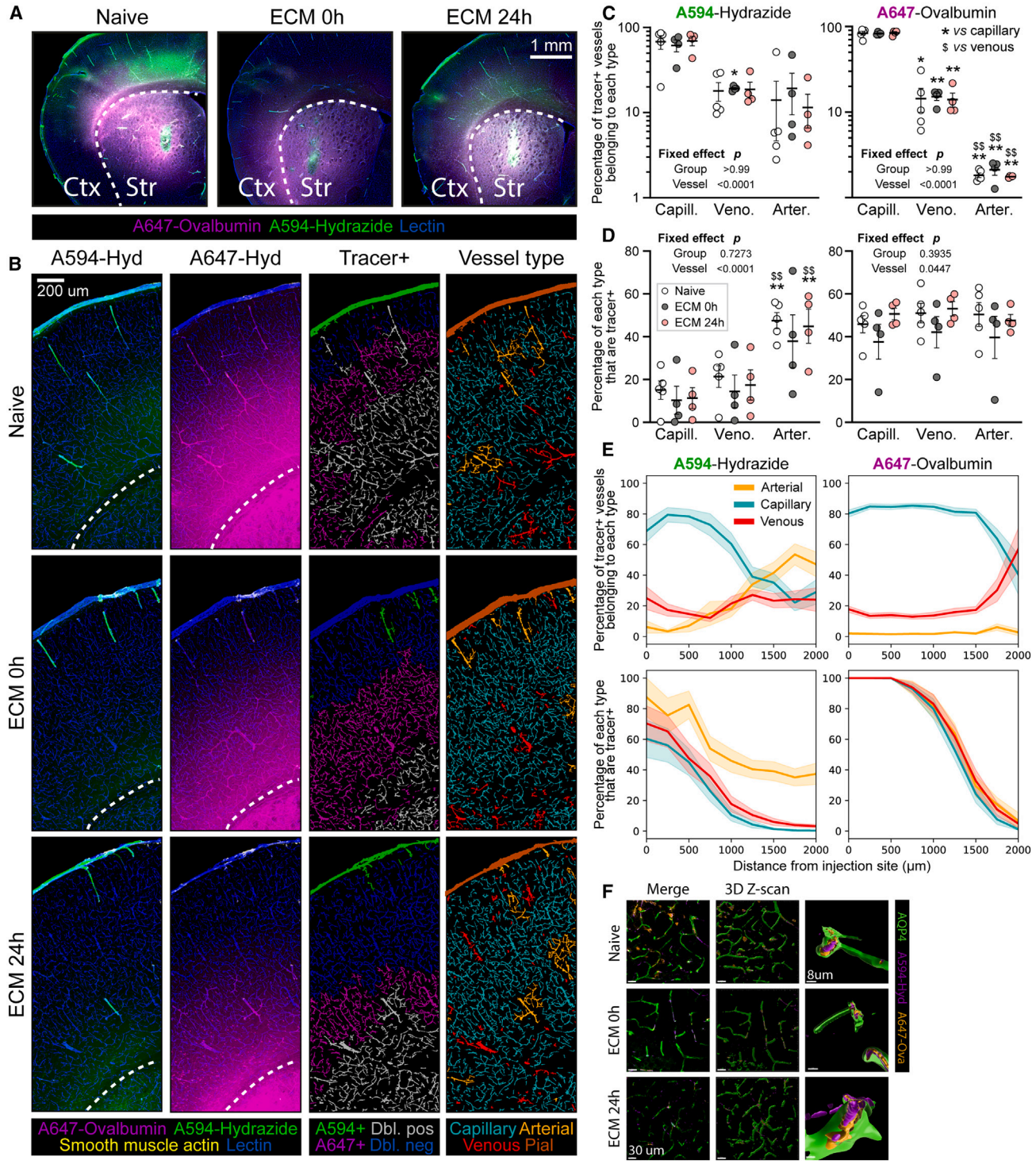

Figure 4. Tracers accumulate within the perivascular spaces of blood vessels during clearance from the brain

Small (Alexa 594-hydrazide) and large (Alexa 647-ovalbumin) tracers were injected into the brain striatum of naive mice, mice with ECM, and to mice 18–24 h post-treatment with artesunate under isoflurane and recovery anesthesia.

(A) Representative images showing the position of the tracers around the striatal (Str) injection site and in the cortex (Ctx) of the brain at 3 h post-injection.

(B) Representative images showing the colocation of the tracers with computationally segmented arteries (lectin$^+$, SMA$^+$), capillaries (lectin$^+$, SMA$^-$, smaller diameter), and veins (lectin$^+$, SMA$^-$, larger diameter) in the striatum and cortex at 3 h post-injection.

(legend continued on next page)

the brains of mice with ECM at 1 h post-injection than in the other groups of mice (Figures 3C and 3D). At 3 h post-injection, the fluorescence intensity of both tracers were significantly lower in brains of mice with ECM than in the other groups of mice, when analyzing macroscopically via stereotaxic microscopy and by standard microscopy in sections surrounding the injection site (Figures 3C and 3D). Notably, there was also a statistically significant faster rate of clearance of both tracers in brains of mice with ECM compared with naive mice and mice following anti-malarial drug treatment (measuring the ratio of tracer in brain at 3 h compared with 1 h), with the exception of the A647 tracer when assessed at the bottom of the brain (Figure 3E). A594-hydrazide appeared to be removed at a relatively faster rate than the A647-ovalbumin from around the injection site in all three groups of mice (Figure 3F), but the A647 tracer was almost entirely removed from naive mice at 24 h post-injection, showing that it was not trapped in the brain parenchyma (Figure S4F). Combined, this suggests that tracers were rapidly removed (and efflux pathways were increased rather than defective) in mice with the established ECM syndrome.

Vasogenic edema fluid and material exit the skull through lymphatic pathways during recovery from ECM

We next examined where the edematous fluid/ISF drained from the cranium during ECM and following anti-malarial drug treatment. Efflux of ISF and edematous fluid along capillaries and arteries has previously been reported in other conditions,[46–48] while ISF and macromolecule efflux along perivenous routes has been postulated within the glymphatic pathway.[16,19,21] Consistent with this, both small and large tracers injected into the brain striatum appeared to accumulate with cerebral blood vessels at 3 h post-injection in all three groups of mice (Figures 4A and 4B). Although there was clear overlap where the small and large tracers colocalized with identified vessels, particularly around the injection site, distinct A647-ovalbumin tracer single-positive and A594-hydrazide tracer single-positive vessels were also identified, with A594-hydrazide single-positive vessels found predominantly at the cortex and brain borders (Figure 4B). The majority of both A647-ovalbumin and A594-hydrazide tracer$^+$ vessels were identified as brain capillaries in naive mice, mice with ECM, and in mice 18–24 h after anti-malarial drug treatment (Figure 4C). The A594-hydrazide tracer appeared to accumulate proportionally to a similar lower level with both veins and arteries, whereas the A647-ovalbumin tracer accumulated at proportionally higher levels with veins compared with SMA$^+$ arteries in all three groups of mice (Figure 4C). When calculating the percentage of each vessel type within the ipsilateral hemisphere that were colocalized with the intrastriatal-injected tracers, a higher percentage of arteries were positive for A594-hydrazide compared with capillaries and veins. In contrast, a similar percentage of capillaries, veins, and arteries were positive for A647-ovlabumin in all three groups of mice (Figure 4D). As suggested in the qualitative images (Figures 4B and S4G), the level of tracer, particularly A594-hydrazide, association with capillaries decreased with distance from the injection site, and the relative level of A594-hydrazide and A647-ovalbumin accumulation with arteries and veins appeared to increase in the cortical and brain border areas, respectively (Figure 4E). Notably, despite the apparent differences in pattern of accumulation with the different vessel types in the brain, the large and small tracers equally crossed the glial limitans (demarcated by AQP4) and entered the vessel paravascular spaces in the different groups of mice (Figure 4F).

As paravascular transport of ISF can potentially route fluid and materials to the CSF containing SAS and subsequently to different lymphatic networks in the cranium,[21–30,49–51] we analyzed the presence of the intrastriatal-injected tracers in the dorsal, basal, and nasal regions of the brain and skull, as well as the spinal cord, which is also a drainage site for CSF (Figure 5A). To assess drainage at these sites, we utilized a rapid decalcification protocol that allowed us to section the skull while preserving epitopes for immunohistochemical labeling, and also the structure of the brain and soft tissues[26] (Figure 5A). We also visualized and quantified the tracers directly in the skull base and skull cap without further tissue processing (Figure S5). Both A594-hydrazine and A647-ovalbumin tracers were clearly observed proximal to the striatal injection site and anterior in or surrounding the olfactory bulb 1 h post-injection in all three groups of mice (Figure 5A). There was significantly increased tracer accumulation at and across the cribriform plate and in the basal brain regions, in the region of the cavernous sinus and nasopharyngeal plexus, compared with the dorsal regions or spine at 1 h post-injection (Figures 5B and 5C). Importantly, there was no evidence of rerouting or change in accumulation pattern of the tracers in the brains of mice with ECM or at 18–24 h after anti-malarial drug treatment, compared with naive mice at 1 h post-injection (Figures 5B and 5C). At 3 h post-injection, tracers were also observed in the anterior skull regions and in the nasal and cribriform regions, as well as the basal brain regions, in all three groups of mice (Figures S5A–S5C). There was, however, a significant decrease in tracer signal in the different CNS locations in mice with the established ECM syndrome when measured at 3 h post-injection (Figure S5D), mirroring the rapid efflux of tracer from the brain parenchyma in that group of mice at that time point (Figure 3) compared with naive mice or in mice recovering from the syndrome after anti-malarial drug administration. There was no evidence of rerouting of tracers to different CNS or skull regions at 3 h post-injection compared

(C and D) Quantification over the entire injected hemisphere (mean of 4,022 vessels analyzed per animal: $n = 4–5$ per group) of (C) the relative percentage of A594-hydrazide and A647-ovalbumin tracer$^+$ vessels that were of each vessel type and (D) the percentage of each vessel type that were tracer$^+$.

(E) The impact of vessel distance from the injection site on vascular analyses, with shaded area showing 95% confidence interval over 14 animals (groups combined).

(F) Representative images and 3D reconstructions showing the location of the two tracers in the perivascular compartment of cerebral vessels in the different groups of mice 3 h post-injection. Statistics for (C) and (D): proportions were transformed using a centered log-ratio transformation, followed by mixed effects model using animal as a random effect, and Tukey's post hoc. *$p < 0.05$, **$p < 0.01$ vs. capillary, \$$p < 0.05$, \$\$$p < 0.01$ vs. venous. Data are presented as mean ± standard error of mean.

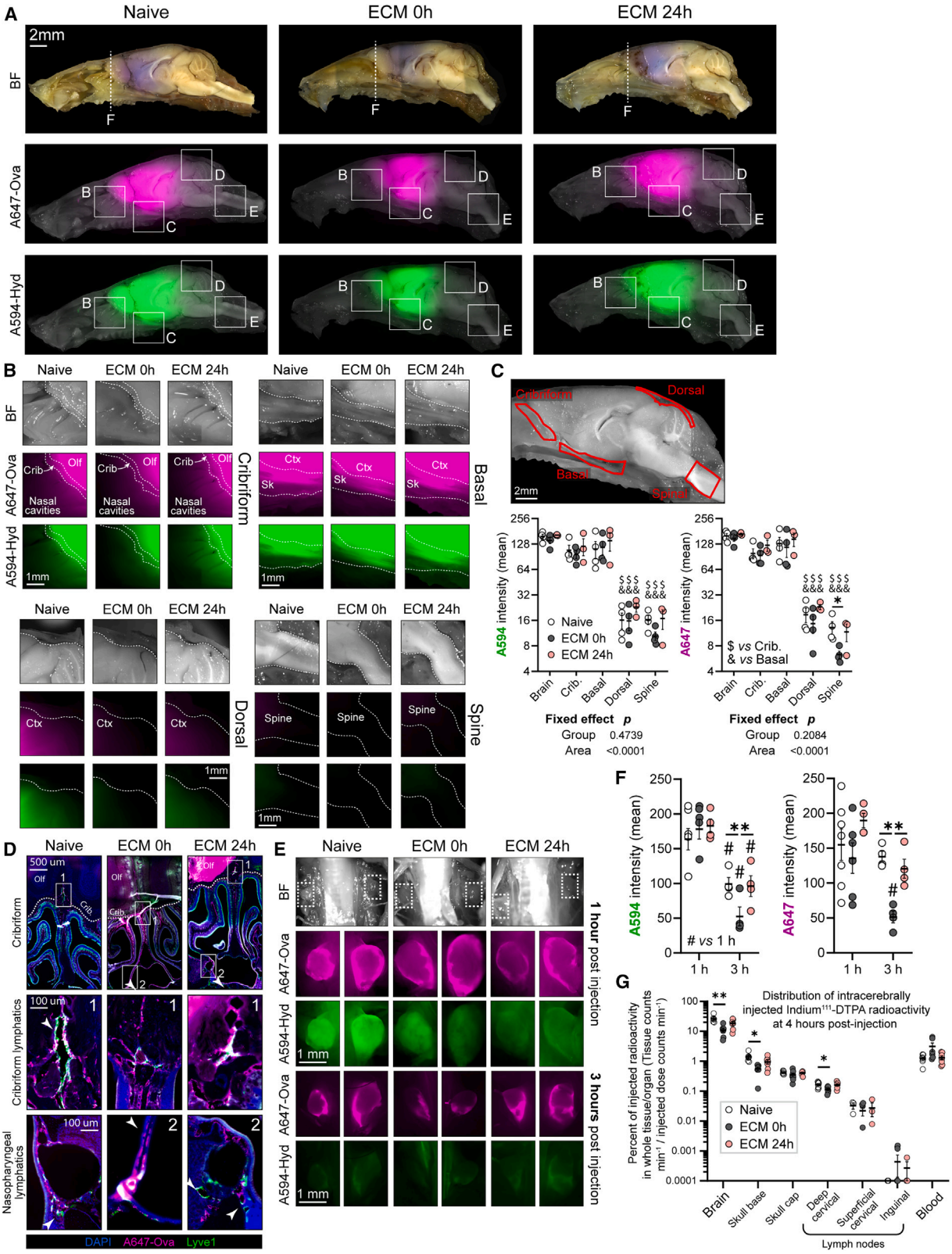

(legend on next page)

with 1 h post-injection in any of the groups of mice (Figures 5 and S5).

Consistent with evidence of tracer traversal through the cribriform plate (Figures 5B and 5C), A647-ovalbumin was observed associated with Lyve-1$^+$ lymphatic vessels passing through the cribriform, and in lymphatic vessels at the base of the nasal cavity associated with the nasopharynx at 1 h post-injection in all three groups of mice (Figure 5D). Background staining in the A647 channel was negligible in cribriform and nasal lymphatic regions in mice that did not receive any tracer injections, whereas autofluorescence in the A594 channel after tissue decalcification prevented accurate tracking of the A594-hydrazide in the nasal compartments (Figures S6A and S6B). In agreement with data in Figures 5B and 5C, A647-ovalbumin tracer accumulation was also observed with Lyve-1$^+$ vessels in the basal compartment (Figure S6C), albeit at qualitatively lower levels than in the nasal fossae, at 1 h post-injection, with no apparent differences in tracer colocalization observed within mice with ECM, at 18–24 h post-treatment and naive mice (Lyve-1$^+$ vessels were clearly distinguished, despite the high background in these regions after tissue decalcification) (Figures 5D and S6C). In agreement with data in Figures 5B and 5C, A647-ovalbumin was found in a very limited amount in the pia or colocalized with Lyve-1$^+$ vessels in the spine, with the detected A647-ovalbumin appearing cellular associated (Figure S6D). To examine any potential drainage of intrastriatal-injected tracers by dorsal lymphatic vessels, we performed dorsal meningeal whole-mount staining. At 3 h post-injection, low levels of A647-ovalbumin tracer was identified associated with anterior Lyve-1$^+$ vessels (putative lymphatic vessels lining the superior sagittal sinus) in the dorsal meninges in all three groups of mice, but was not identified associated with larger Lyve-1$^+$ dorsal lymphatic vessels at the sinus confluence or in location of the transverse sinus (Figure S6E). The diameter of dorsal lymphatic vessels lining the superior sagittal sinus was unaltered in mice with ECM and at 18–24 h after anti-malarial drug treatment compared with naive mice, suggesting that the acute ECM syndrome did not affect the architecture of the dorsal lymphatic network (Figures S7A and S7B). There was, however, a significant increase in the numbers of CD45$^+$ leukocytes in vicinity with dorsal lymphatic vessels in mice at 18–24 h after anti-malarial drug treatment of ECM compared with naive mice (Figures S7A and S7C), showing that the dorsal meninges is immunologically active during the recovery from the syndrome.

The nasal and basal lymphatic networks drain predominantly to the dcLNs.[21–30,49–51] In agreement with the accumulation of intrastriatal-injected tracers in the vicinity of the dorsal, basal, and nasal lymphatic networks in naive mice, mice with ECM, and in mice treated with anti-malarial drugs (Figures 5A–5D), there was clear evidence of tracer drainage to the dcLNs in all groups of mice at 1 h after intrastriatal injection (Figure 5E). The larger A647-ovalbumin tracer was predominantly localized in the subcapsular sinus regions, whereas the small A594-hydrazine tracer was diffusely spread throughout the dcLN (Figure 5E). While the levels of the tracers were comparable in the three groups of mice at 1 h post-injection, there was a significant reduction in tracer intensity in the dcLN in mice with ECM at 3 h post-injection, compared with levels in naive mice and in mice 18–24 h after anti-malarial drug treatment (Figure 5F). This is consistent with the lower levels of residual tracer in the brain parenchyma of mice with ECM at 3 h post-intrastriatal injection (Figure 3). Indeed, although the levels of A594-hydrazide was significantly lower in the dcLNs in all three groups of mice at 3 h post-intrastriatal injection compared with 1 h post-injection, this reduction was most pronounced in the mice with ECM (Figure 5F). Similarly, while the levels of A647-ovalbumin trended lower in the dcLNs of naive mice and in mice at 18–24 h after anti-malarial drug treatment at 3 h post-injection compared with levels at 1 h post-injection, this was only significantly different in mice with ECM (Figure 5F). As expected, based on the almost complete removal of tracers from the brain 24 h post-injection into the striatum (Figure S4F), both A647-ovalbumin and A594-hydrazide were observed at very low levels in the dcLNs of naive mice 24 h post-injection (Figure S7D), showing that tracers were not trapped in the dcLNs long term after drainage from the brain.

To confirm the CNS efflux pathways identified using fluorescent tracers, we injected the small radionuclide ^{111}In-DTPA into the striatum of naive mice, mice with ECM, and mice recovering from the syndrome 18–24 h following anti-malarial drug treatment. In all three groups of mice, radionuclide was identified (4 h after injection) draining to the skull base and skull cap and entering the dcLNs (Figure 5G). While some radionuclide was detected in the superficial cervical lymph nodes, this was substantially lower than in the dcLNs (Figure 5G). No tracer was observed in non-CNS-draining lymph nodes (inguinal as example). Radionuclide was also observed in the blood (to high level when calculating the level in the entire mouse blood volume) (Figure 5G). Consistent with our earlier observations using fluorescent tracers (Figures 3 and S5), we also observed lower levels

Figure 5. The route of fluid and macromolecule clearance from the cranium in mice with ECM

Small (Alexa 594-hydrazide) and large (Alexa 647-ovalbumin) tracers were injected into the striatum of naive mice, mice with ECM, and to mice 18–24 h post-treatment with artesunate under isoflurane and recovery anesthesia.

(A) Representative images of decalcified skulls cut at the midline showing tracer position within the skull at 1 h post-injection.

(B) Representative images (from selected regions in A) showing tracer accumulation around the cribriform plate, basal brain compartment, dorsal brain region, and the opening to the spinal canal at 1 h post-injection.

(C) Quantification of tracer accumulation in anatomical sites of tracer egress from the skull. n = 3–4, mixed effects model with Tukey's post hoc test ($\$p < 0.05$ vs. cribriform $\&p < 0.05$ vs. basal).

(D) Tracer accumulation proximal to Lyve-1+ vessels (white arrows) at the cribriform plate (dotted line) and associated with the nasopharynx at 1 h post-injection.

(E and F) (E) Representative images and (F) quantification showing the accumulation of tracers in the dcLNs at 1 and 3 h post-intracerebral injection into naive mice, mice with ECM, and in mice 18–24 h after anti-malarial drug treatment. n = 4–7, two-way ANOVA with Tukey's post hoc ($\#p < 0.05$ for 3 vs. 1 h).

(G) Calculated percentage of injected dose of ^{111}In-DTPA within the specified organs and CNS components 4 h post-intracerebral (striatum) injection into naive mice, mice with ECM, and mice 18–24 h post-administration of anti-malarial drugs. Mixed effects statistical model with Tukey's post hoc test, n = 6–7. Statistics for (C), (F), and (G); $^*p < 0.05$, $^{**}p < 0.01$, $^{***}p < 0.001$, $^{****}p < 0.0001$. Data are presented as mean ± standard error of mean.

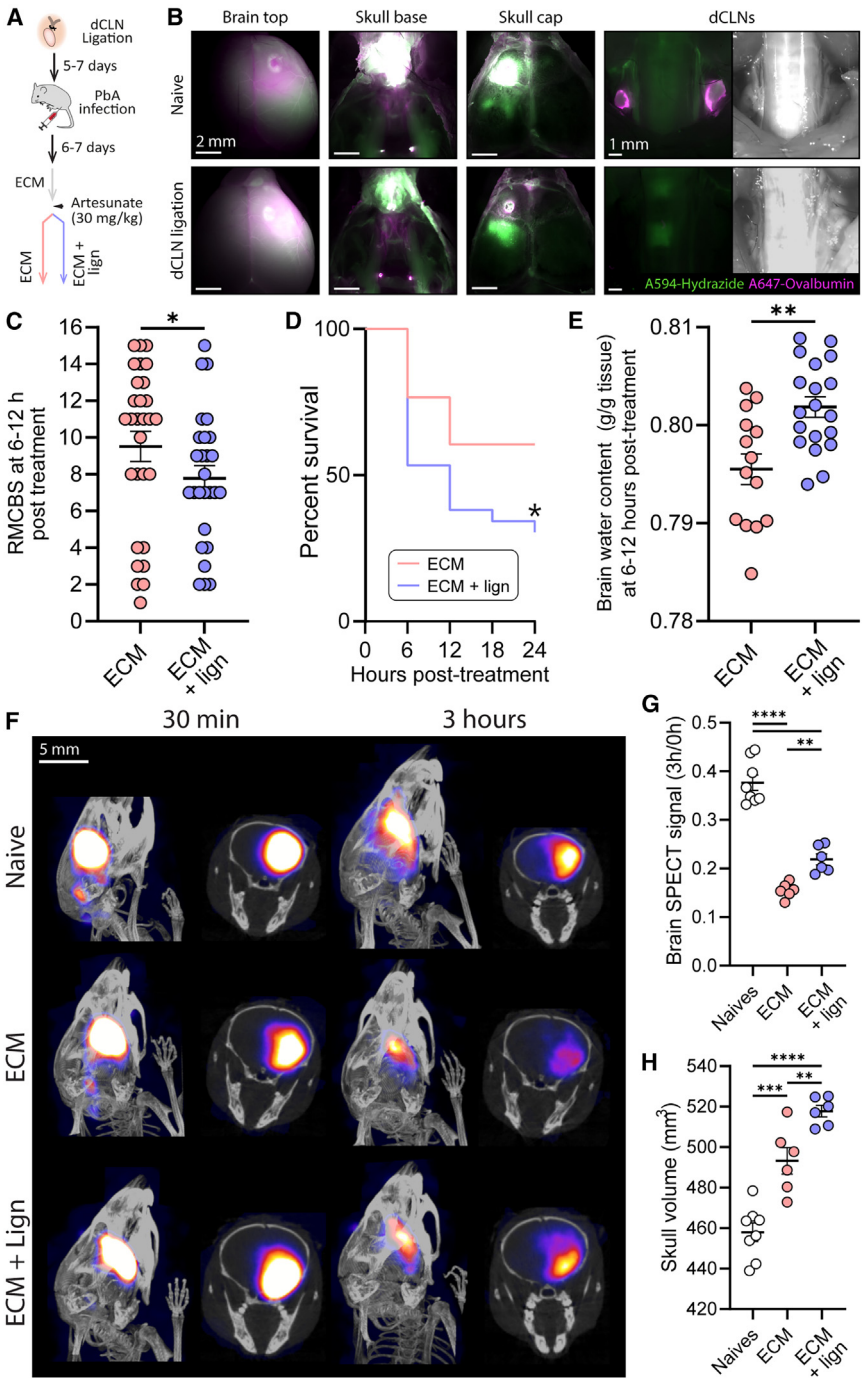

Figure 6. Recovery from ECM and resolution of vasogenic edema depends upon drainage to the dcLNs

(A) The experimental design to assess how ligation of lymphatic vessels afferent to dcLNs influences anti-malarial drug treatment of established ECM.

(B) Representative images showing Alexa 594 and Alexa 647 expression and localization 3 h post-injection within the brain parenchyma of naive mice and mice following surgical ligation of lymphatic vessels draining to dcLNs (performed 5–7 days post-surgery).

(C and D) (C) RMCBS score at 6–12 h post-treatment and (D) survival of control mice and mice with ligation of lymphatic vessels afferent to dcLNs following anti-malarial drug treatment of established ECM. Mann-Whitney U and log rank (Mantel-Cox) tests, n = 27–29.

(E) Brain water content in control mice and mice with ligated lymphatic vessels draining to dcLNs, both 6–12 h after anti-malarial drug treatment of ECM. Mann-Whitney U test, n = 14–19.

(F and G) (F) Representative SPECT-CT images showing and (G) calculated level of ^{111}In-DTPA in brains of mice 30 min and 3 h post-injection into the striatum, with injection performed at time point of anti-malarial drug treatment of established ECM under isofluorane anesthesia.

(H) Skull volume, calculated from CT imaging, in control mice and mice with surgical ligation of lymphatic vessels afferent to dcLNs, both 3 h after anti-malarial drug treatment. Statistics for (G) and (H) were one-way ANOVA with Tukey's post hoc, n = 6–8. (C–E, G–H) $^{*}p < 0.05$, $^{**}p < 0.01$, $^{***}p < 0.001$, $^{****}p < 0.0001$. Data are presented throughout as mean ± standard error of mean.

of ^{111}In-DTPA within the brain parenchyma, skull base, and dcLN locations in mice with ECM than in naive mice at 4 h post-injection, although levels in the blood trended higher in mice with ECM, suggesting that the radionuclide drained faster to the blood in mice with ECM (Figure 5J).

Taken together, these data indicate that vasogenic edema fluid and macromolecules (differentially assessed using small and large tracers, respectively), appeared to exit the brain parenchyma from the parenchyma to the PVS for efflux to the nasal and basal lymphatic networks for subsequent drainage out of the cranium to the dcLNs. These drainage pathways appeared to operate more efficiently to drain fluid and materials from the cranium during ECM.

Vasogenic edema clearance through the dcLNs is essential for effective recovery from ECM

To directly analyze the importance of CNS lymphatic networks for the clearance of edema and recovery from ECM, we ligated the afferent lymphatic vessels draining to the dcLNs, as performed previously[52] (Figure 6A). Ligation of dcLNs was effective at preventing intrastriatal injected tracer draining to the dcLNs (Figure 6B). As reported previously,[52] short-term ligation of the afferent lymphatic vessels draining to the dcLNs did not affect brain water content in naive mice (Figure S8A). While ligation of dcLNs did not significantly alter the kinetics of ECM development (based upon RMCBS monitoring) (Figure S8B), with all mice treated with anti-malarial drugs at 11–12 on the RMCBS

scale, ligation significantly reduced the RMCBS score in mice 6–12 h after anti-malarial drug treatment (when brain water content reaches maximal following anti-malarial drug treatment; Figure 1G) and significantly reduced survival of mice after drug treatment (Figures 6C and 6D). Critically, ligation of the afferent lymphatic vessels draining to the dcLNs also significantly reduced the capacity of mice to control brain water content in the acute 6-h period after anti-malarial drug treatment (Figure 6E). Consistent with data during development of ECM (Figure 1B), there was a strong inverse correlation between RMCBS and brain water content in control mice and mice with ligated afferent lymphatic vessels draining to the dcLNs (Figure S8C). Through SPECT-CT analyses, we confirmed that the inability of mice to control brain water following dcLN ligation was due to reduced capacity to clear fluid from the brain during acute recovery from the syndrome (Figures 6F and 6G), and failure to control brain volume (Figure 6H). Together, these data show that drainage of fluid to the dcLNs is a critical pathway underpinning recovery from ECM.

DISCUSSION

In this study, we have examined the kinetics and routes of fluid removal from the brain in mice with ECM and following anti-malarial drug treatment of the syndrome. We have demonstrated the importance of CNS lymphatic networks for effective recovery from ECM and have shown that prevention of fluid drainage to the CNS draining dcLNs significantly reduces the capacity to regulate brain water content and volume, which impairs anti-malarial drug treatment success and recovery from the syndrome.

We have shown that the murine ECM model, comparable with pediatric CM,[5–10] is associated with a significant increase in brain water content and brain swelling, and identified that anti-malarial drug treatment did not immediately close the BBB or limit edema. Notably, vascular leakage did not directly correspond with local endothelial cell activation (as defined by ICAM-1 expression) and, as in pediatric CM,[53] endothelial cell activation persisted after repair of the BBB. As such, although endothelial cell activation and BBB leakage have been linked macroscopically during CM,[6,14] more investigations are required to investigate the factors influencing BBB damage on a vessel-per-vessel basis.

The kinetics of fluid accumulation and sustained BBB dysfunction in the acute time period after anti-malarial drug administration provides a potential explanation for the sub-optimal efficacy of artesunate for treatment of ECM, where, as in pediatric HCM, survival or death is determined within 24 h post-treatment.[11] The fact that increased fluid accumulation and brain swelling was still observed for a period of time after anti-malarial drug treatment and subsequent closure of the BBB (even when brain endothelial cells remain highly inflamed) may also help explain the observations of vasogenic edema without signs of apparent BBB disruption in some MRI studies of children with HCM.[8]

It was interesting that CSF influx into the brain was disrupted in mice with the established ECM syndrome and extant BBB dysfunction, whereas CSF flow was significantly upregulated as the BBB was repaired and vasogenic edema began to clear. Potential pathological factors that may repress CSF flow during ECM, include brain swelling and collapse of the SAS, hemostasis, and loss of arterial pulsatility, hyperlactemia, hypercapnia, and respiratory distress,[16,19,54–56] although these hypotheses require experimental validation. Irrespective, alterations in PVS accessibility, or repolarization of AQP4, which are major causes of reduced CSF perfusion in other models,[16,19,38,54] was unlikely to contribute to impaired CSF flow during ECM or following anti-malarial drug administration. Instead, our results are consistent with a model where influx of blood products into the PVS compartment due to BBB damage and vasogenic edema during ECM creates pressure (hydrostatic and/or osmotic) within the PVS compartment that inhibits CSF influx via perivascular pathways. This may backup CSF within the restricted SAS, possibly redirecting CSF clearance to bypass parenchyma perfusion.[57,58] As the BBB resealed and vasogenic fluid quickly drained from the cranium 12–24 h after anti-malarial drug treatment, ICP rapidly lowered, which, combined with reengaged vascular perfusion, enabled the CSF to flow rapidly down the enlarged PVS (observed histologically and by IF analyses), entering into the brain parenchyma. In agreement with this model, inhibition of vasogenic edema rapidly re-established CSF perfusion in other diseases.[59] Consequently, the rapid CSF influx did not appear to sustain or exacerbate edema during recovery from ECM, as in stroke,[37] but was potentially important for cleansing the brain parenchyma, reducing neuroinflammation and allowing the rapid return of brain health.[17,52,60]

In direct contrast with the disruption in CSF flow in mice with established ECM, the fluid and macromolecule clearance systems in the brain appeared to be upregulated in mice at the time point of anti-malarial drug treatment. This was demonstrated by significantly increased efflux of intracerebral injected high- and low-weight fluorescent tracers and radionuclides from the brains of mice with ECM than in naive mice or in mice 18–24 h after° anti-malarial drug treatment of the syndrome. Our results are consistent with the view that vasogenic edema fluid may move to the low-resistance PVS around cerebral vessels for likely removal to the subarachnoid CSF space, as has been shown previously for removal for ISF in other models.[19,61–64] Given that tracers injected into the brain striatum were observed within the PVS/basement membranes of capillaries, veins, and arteries in all three groups of mice, the relative importance of efflux along perivenous routes (proposed within the glymphatic pathway[21,54]), versus periarterial and capillary-associated clearance pathways[46–48] is, however, unclear. Moreover, our analyses suggest that different sized tracers may efflux the brain at different rates and with subtle differences in preference for different vessel types. As such, the role of bulk fluid flow for the removal of edematous fluid and macromolecules from the brains of mice with ECM and during the recovery from the syndrome requires additional investigation.

How ECM-related pathologic events and alterations in brain water content promotes increased efficiency of brain waste clearance warrants further investigation. Indeed, while some studies have indicated that raised ICP promotes CSF removal,[65,66] other studies have shown this prevents clearance of edematous fluid and CSF.[44,45,67] Nevertheless, our results, obtained employing an isofluorane and recovery anesthesia regimen optimized to assess physiologic solute efflux from the brain parenchyma,[55]

do show that the rapid onset of edema and brain swelling during ECM is not due to widespread and catastrophic blockage of fluid drainage, or disordered expression or polarization of AQP4. AQP4 has been shown to promote the removal of vasogenic edema fluid following damage to the BBB in other models.[41] Instead, our data indicate that the rapid accumulation of fluid and associated brain swelling is due to influx pathways overwhelming CNS clearance systems.

Following clearance from the brain parenchyma, we observed injected fluorescent tracers and radionuclides at quantitatively highest levels at the base of the skull and proximal to the cribriform plate and nasopharyngeal lymphatic Lyve-1$^+$ vessels in mice with ECM and following anti-malarial drug treatment. Although some tracer was observed dorsally within the meninges, this was anterior and away from the lymphatic vessels adjacent to the transverse sinus, where the main access points to the dorsal lymphatic network are located.[68] While the nasal lymphatics may not be anatomically connected with the meningeal lymphatics,[29] both networks converge through the nasopharyngeal plexus to drain to the dcCLNs.[22,23,27,30] Consistent with this, we also saw intrastriatal-injected tracers rapidly draining to the dcLNs within 1 h post-injection in all three groups of mice. The quantitatively lower quantities of tracer observed in the dcLNs of mice with ECM at 3 h post-injection was likely directly reflective of the low levels of tracers in the brain parenchyma in this group at this time point. Indeed, fluorescent tracers and small inert molecules draining from the skull generally egress through lymphatic vessels and lymph nodes very quickly,[22,27] and can pass through a lymph node at a speed of up to 10 mm/min (within an LN of diameter < 2 mm), effectively clearing lymph nodes in <15 min.[69–71] Dynamic intravital microscopy comparing the tracer clearance rates through the dcLNs to the blood in the three groups of mice would be required to confirm this hypothesis. We did not observe substantial redirection of fluid drainage via alternative routes in mice with ECM, such as clearance via the spinal cord.[26,45,65,72,73] Critically, ligation of the lymphatic vessels draining to the dcLNs significantly impaired fluid clearance from the brain. As such, our results indicate that, in mice with ECM and during recovery from the syndrome, a significant proportion of vasogenic edema fluid and macromolecules associate with and exit via the basal and nasal submucosa lymphatic networks to the dcLNs. In agreement with this view, perineural outflow along the olfactory nerves through foramina in the cribriform plate, which also contain lymphatic vessels, to the nasal lymphatics have been shown to be major egress sites for CSF.[26–30,74]

Limitations of the study

Whether the choice of anesthesia in our study exacerbated or reduced the individual impact of pathological features associated with ECM on CSF flow is unclear, but we employed an anesthesia regimen (ketamine/xylazine) validated for sensitive and quantitative assessment of CSF flow, particularly influx into the brain.[55] While we observed clear enlargement of PVSs in the brains of mice with ECM, as has previously been observed in murine and human CM,[39,75–77] PVSs are known to collapse postmortem following perfusion and fixation.[78] As such, our results may underrepresent the magnitude of PVS expansion across the cerebrovascular network during ECM and in mice 18–24 h post-treatment of the syndrome. We also acknowledge that our analyses of CSF penetration into the penetrating vessels and brain parenchyma of mice at 18–24 h post-treatment may also be influenced through the use of postmortem samples.[57] As we were unable to successfully perform intracerebral injections at 6 h after anti-malarial drug treatment of ECM, when brain water content and ICP are highest, due to tracer reflux and/or animals failing to survive the surgical procedure, we cannot fully discount that drainage pathways were not transiently disrupted at the peak of cerebral edema during ECM. Moreover, as we were unable to perform intraparenchymal injections into mice that failed anti-malarial drug treatment (due to treatment success or failure only being robustly identified after 6 h post-treatment), we were not able to directly assess if the efficiency of brain efflux pathways differed in successfully treated mice or mice that failed to recover.

Overall, we have provided insight into how the brain recovers from ECM and, in particular, how fluid is drained from the cranium and brain swelling is controlled. As many of the lymphatic pathways and systems appear to be conserved, and have equivalent functions, in humans and in mice,[29,49] we expect that our results in the ECM model will be translationally relevant for human CM, and for other conditions associated with extensive vasogenic edema. Critically, as we show that fluid influx into the brain does not immediately cease after anti-malarial drug treatment, and egress pathways are significantly upregulated during ECM, our results suggest that adjunctive therapies that quickly repair the integrity of the BBB hold the greatest potential for improving treatment success of CM.

STAR★METHODS

Detailed methods are provided in the online version of this paper and include the following:

- KEY RESOURCES TABLE
- RESOURCE AVAILABILITY
  - Lead contact
  - Materials availability
  - Data and code availability
- EXPERIMENTAL MODEL AND STUDY PARTICIPANT DETAILS
- METHOD DETAILS
  - *Plasmodium berghei* ANKA infection and tissue preparation
  - Assessing brain water content
  - Administration of FITC-albumin to visualise blood-brain barrier breakdown
  - Administration of tracers via cisterna magna injection
  - Administration of tracers via intracerebral injection
  - Stereomicroscopy
  - Laser speckle
  - Ligation of afferent lymphatic vessels draining to dcLNs
  - Single-Photon emission computerised tomography (SPECT)/CT
  - Immunohistochemistry and image analysis
  - Decalcification of skulls
- QUANTIFICATION AND STATISTICAL ANALYSIS

SUPPLEMENTAL INFORMATION

Supplemental information can be found online at https://doi.org/10.1016/j.celrep.2024.114217.

ACKNOWLEDGMENTS

We thank Dr Peter March and the BioImaging Core Facility at the University of Manchester for enabling the microscopy experiments performed in this study. We thank the Biological Services Facility at the University of Manchester for help with animal work. We thank Dr Igor Smirnov, Washington University School of Medicine in St Louis, for protocol advice on ligation of afferent lymphatic vessels draining to dcLNs. The study was supported by the Medical Research Council (MR/R010099/1 to K.N.C., A.G.C., and D.B., MR/V034650/1 to K.N.C. and B.D., and MR/T016515/1 to D.B. and K.N.C.). MR/R010099/1 was jointly funded by the UK Medical Research Council (MRC) and the UK Department for International Development (DFID) under the MRC/DFID Concordat agreement and was also part of the EDCTP2 program supported by the European Union.

AUTHOR CONTRIBUTIONS

M.J.H., R.B., D.A.J., J.G., and M.H. performed the experiments. M.J.H., R.B., and M.H. analyzed the data. M.J.H., B.D., A.G.C., D.B., and K.N.C. designed the study. M.J.H., R.B., and K.N.C. wrote and edited the manuscript. B.D., A.G.C., D.B., and K.N.C. obtained funding for the work.

DECLARATION OF INTERESTS

The authors declare no competing interests.

Received: November 22, 2022
Revised: November 29, 2023
Accepted: April 25, 2024
Published: May 9, 2024

REFERENCES

1. World Health Organisation (2021). World malaria report. https://www.who.int/teams/global-malaria-programme/reports/world-malaria-report-2021.
2. Schiess, N., Villabona-Rueda, A., Cottier, K.E., Huether, K., Chipeta, J., and Stins, M.F. (2020). Pathophysiology and neurologic sequelae of cerebral malaria. Malar. J. *19*, 266.
3. Christensen, S.S., and Eslick, G.D. (2015). Cerebral malaria as a risk factor for the development of epilepsy and other long-term neurological conditions: a meta-analysis. Trans. R. Soc. Trop. Med. Hyg. *109*, 233–238.
4. Rosa-Goncalves, P., Ribeiro-Gomes, F.L., and Daniel-Ribeiro, C.T. (2022). Malaria Related Neurocognitive Deficits and Behavioral Alterations. Front. Cell. Infect. Microbiol. *12*, 829413.
5. Seydel, K.B., Kampondeni, S.D., Valim, C., Potchen, M.J., Milner, D.A., Muwalo, F.W., Birbeck, G.L., Bradley, W.G., Fox, L.L., Glover, S.J., et al. (2015). Brain swelling and death in children with cerebral malaria. N. Engl. J. Med. *372*, 1126–1137.
6. Frevert, U., and Nacer, A. (2014). Fatal cerebral malaria: a venous efflux problem. Front. Cell. Infect. Microbiol. *4*, 155.
7. Sahu, P.K., Duffy, F.J., Dankwa, S., Vishnyakova, M., Majhi, M., Pirpamer, L., Vigdorovich, V., Bage, J., Maharana, S., Mandala, W., et al. (2021). Determinants of brain swelling in pediatric and adult cerebral malaria. JCI Insight *6*, e145823.
8. Potchen, M.J., Kampondeni, S.D., Seydel, K.B., Haacke, E.M., Sinyangwe, S.S., Mwenechanya, M., Glover, S.J., Milner, D.A., Zeli, E., Hammond, C.A., et al. (2018). 1.5 Tesla Magnetic Resonance Imaging to Investigate Potential Etiologies of Brain Swelling in Pediatric Cerebral Malaria. Am. J. Trop. Med. Hyg. *98*, 497–504.
9. Sahu, P.K., Hoffmann, A., Majhi, M., Pattnaik, R., Patterson, C., Mahanta, K.C., Mohanty, A.K., Mohanty, R.R., Joshi, S., Mohanty, A., et al. (2021). Brain Magnetic Resonance Imaging Reveals Different Courses of Disease in Pediatric and Adult Cerebral Malaria. Clin. Infect. Dis. *73*, e2387–e2396.
10. Mohanty, S., Benjamin, L.A., Majhi, M., Panda, P., Kampondeni, S., Sahu, P.K., Mohanty, A., Mahanta, K.C., Pattnaik, R., Mohanty, R.R., et al. (2017). Magnetic Resonance Imaging of Cerebral Malaria Patients Reveals Distinct Pathogenetic Processes in Different Parts of the Brain. mSphere *2*. e00193-17.
11. Dorovini-Zis, K., Schmidt, K., Huynh, H., Fu, W., Whitten, R.O., Milner, D., Kamiza, S., Molyneux, M., and Taylor, T.E. (2011). The neuropathology of fatal cerebral malaria in malawian children. Am. J. Pathol. *178*, 2146–2158.
12. Patnaik, J.K., Das, B.S., Mishra, S.K., Mohanty, S., Satpathy, S.K., and Mohanty, D. (1994). Vascular clogging, mononuclear cell margination, and enhanced vascular permeability in the pathogenesis of human cerebral malaria. Am. J. Trop. Med. Hyg. *51*, 642–647.
13. Brown, H., Hien, T.T., Day, N., Mai, N.T., Chuong, L.V., Chau, T.T., Loc, P.P., Phu, N.H., Bethell, D., Farrar, J., et al. (1999). Evidence of blood-brain barrier dysfunction in human cerebral malaria. Neuropathol. Appl. Neurobiol. *25*, 331–340.
14. Brown, H., Rogerson, S., Taylor, T., Tembo, M., Mwenechanya, J., Molyneux, M., and Turner, G. (2001). Blood-brain barrier function in cerebral malaria in Malawian children. Am. J. Trop. Med. Hyg. *64*, 207–213.
15. Kampondeni, S., Seydel, K.B., Zhang, B., Small, D.S., Birbeck, G.L., Hammond, C.A., Chilingulo, C., Taylor, T.E., and Potchen, M.J. (2020). Amount of Brain Edema Correlates With Neurologic Recovery in Pediatric Cerebral Malaria. Pediatr. Infect. Dis. J. *39*, 277–282.
16. Rasmussen, M.K., Mestre, H., and Nedergaard, M. (2022). Fluid transport in the brain. Physiol. Rev. *102*, 1025–1151.
17. Louveau, A., Plog, B.A., Antila, S., Alitalo, K., Nedergaard, M., and Kipnis, J. (2017). Understanding the functions and relationships of the glymphatic system and meningeal lymphatics. J. Clin. Invest. *127*, 3210–3219.
18. Weller, R.O., Djuanda, E., Yow, H.Y., and Carare, R.O. (2009). Lymphatic drainage of the brain and the pathophysiology of neurological disease. Acta Neuropathol. *117*, 1–14.
19. Plog, B.A., and Nedergaard, M. (2018). The Glymphatic System in Central Nervous System Health and Disease: Past, Present, and Future. Annu. Rev. Pathol. *13*, 379–394.
20. Proulx, S.T. (2021). Cerebrospinal fluid outflow: a review of the historical and contemporary evidence for arachnoid villi, perineural routes, and dural lymphatics. Cell. Mol. Life Sci. *78*, 2429–2457.
21. Iliff, J.J., Wang, M., Liao, Y., Plogg, B.A., Peng, W., Gundersen, G.A., Benveniste, H., Vates, G.E., Deane, R., Goldman, S.A., et al. (2012). A paravascular pathway facilitates CSF flow through the brain parenchyma and the clearance of interstitial solutes, including amyloid beta. Sci. Transl. Med. *4*, 147ra111.
22. Aspelund, A., Antila, S., Proulx, S.T., Karlsen, T.V., Karaman, S., Detmar, M., Wiig, H., and Alitalo, K. (2015). A dural lymphatic vascular system that drains brain interstitial fluid and macromolecules. J. Exp. Med. *212*, 991–999.
23. Ahn, J.H., Cho, H., Kim, J.H., Kim, S.H., Ham, J.S., Park, I., Suh, S.H., Hong, S.P., Song, J.H., Hong, Y.K., et al. (2019). Meningeal lymphatic vessels at the skull base drain cerebrospinal fluid. Nature *572*, 62–66.
24. Louveau, A., Smirnov, I., Keyes, T.J., Eccles, J.D., Rouhani, S.J., Peske, J.D., Derecki, N.C., Castle, D., Mandell, J.W., Lee, K.S., et al. (2015). Structural and functional features of central nervous system lymphatic vessels. Nature *523*, 337–341.
25. Smyth, L.C.D., Xu, D., Okar, S.V., Dykstra, T., Rustenhoven, J., Papadopoulos, Z., Bhasiin, K., Kim, M.W., Drieu, A., Mamuladze, T., et al. (2024). Identification of direct connections between the dura and the brain. Nature *627*, 165–173.
26. Norwood, J.N., Zhang, Q., Card, D., Craine, A., Ryan, T.M., and Drew, P.J. (2019). Anatomical basis and physiological role of cerebrospinal fluid transport through the murine cribriform plate. Elife *8*, e44278.
27. Ma, Q., Ineichen, B.V., Detmar, M., and Proulx, S.T. (2017). Outflow of cerebrospinal fluid is predominantly through lymphatic vessels and is reduced in aged mice. Nat. Commun. *8*, 1434.
28. Spera, I., Cousin, N., Ries, M., Kedracka, A., Castillo, A., Aleandri, S., Vladymyrov, M., Mapunda, J.A., Engelhardt, B., Luciani, P., et al. (2023).

Open pathways for cerebrospinal fluid outflow at the cribriform plate along the olfactory nerves. EBioMedicine *91*, 104558.

29. Jacob, L., de Brito Neto, J., Lenck, S., Corcy, C., Benbelkacem, F., Geraldo, L.H., Xu, Y., Thomas, J.M., El Kamouh, M.R., Spajer, M., et al. (2022). Conserved meningeal lymphatic drainage circuits in mice and humans. J. Exp. Med. *219*, e20220035.
30. Yoon, J.H., Jin, H., Kim, H.J., Hong, S.P., Yang, M.J., Ahn, J.H., Kim, Y.C., Seo, J., Lee, Y., McDonald, D.M., et al. (2024). Nasopharyngeal lymphatic plexus is a hub for cerebrospinal fluid drainage. Nature *625*, 768–777.
31. Strangward, P., Haley, M.J., Albornoz, M.G., Barrington, J., Shaw, T., Dookie, R., Zeef, L., Baker, S.M., Winter, E., Tzeng, T.C., et al. (2018). Targeting the IL33-NLRP3 axis improves therapy for experimental cerebral malaria. Proc. Natl. Acad. Sci. USA *115*, 7404–7409.
32. Strangward, P., Haley, M.J., Shaw, T.N., Schwartz, J.M., Greig, R., Mironov, A., de Souza, J.B., Cruickshank, S.M., Craig, A.G., Milner, D.A., Jr., et al. (2017). A quantitative brain map of experimental cerebral malaria pathology. PLoS Pathog. *13*, e1006267.
33. Riggle, B.A., Sinharay, S., Schreiber-Stainthorp, W., Munasinghe, J.P., Maric, D., Prchalova, E., Slusher, B.S., Powell, J.D., Miller, L.H., Pierce, S.K., and Hammoud, D.A. (2018). MRI demonstrates glutamine antagonist-mediated reversal of cerebral malaria pathology in mice. Proc. Natl. Acad. Sci. USA *115*, E12024–E12033.
34. Riggle, B.A., Miller, L.H., and Pierce, S.K. (2020). Desperately Seeking Therapies for Cerebral Malaria. J. Immunol. *204*, 327–334.
35. Varo, R., Crowley, V.M., Sitoe, A., Madrid, L., Serghides, L., Kain, K.C., and Bassat, Q. (2018). Adjunctive therapy for severe malaria: a review and critical appraisal. Malar. J. *17*, 47.
36. Ghazanfari, N., Mueller, S.N., and Heath, W.R. (2018). Cerebral Malaria in Mouse and Man. Front. Immunol. *9*, 2016.
37. Mestre, H., Du, T., Sweeney, A.M., Liu, G., Samson, A.J., Peng, W., Mortensen, K.N., Stæger, F.F., Bork, P.A.R., Bashford, L., et al. (2020). Cerebrospinal fluid influx drives acute ischemic tissue swelling. Science *367*, eaax7171.
38. Mestre, H., Hablitz, L.M., Xavier, A.L., Feng, W., Zou, W., Pu, T., Monai, H., Murlidharan, G., Castellanos Rivera, R.M., Simon, M.J., et al. (2018). Aquaporin-4-dependent glymphatic solute transport in the rodent brain. Elife *7*, e40070.
39. Ampawong, S., Combes, V., Hunt, N.H., Radford, J., Chan-Ling, T., Pongponratn, E., and Grau, G.E.R. (2011). Quantitation of brain edema and localisation of aquaporin 4 expression in relation to susceptibility to experimental cerebral malaria. Int. J. Clin. Exp. Pathol. *4*, 566–574.
40. Ren, Z., Iliff, J.J., Yang, L., Yang, J., Chen, X., Chen, M.J., Giese, R.N., Wang, B., Shi, X., and Nedergaard, M. (2013). Hit & Run' model of closed-skull traumatic brain injury (TBI) reveals complex patterns of post-traumatic AQP4 dysregulation. J. Cereb. Blood Flow Metab. *33*, 834–845.
41. Papadopoulos, M.C., and Verkman, A.S. (2013). Aquaporin water channels in the nervous system. Nat. Rev. Neurosci. *14*, 265–277.
42. Newton, C.R., Kirkham, F.J., Winstanley, P.A., Pasvol, G., Peshu, N., Warrell, D.A., and Marsh, K. (1991). Intracranial pressure in African children with cerebral malaria. Lancet *337*, 573–576.
43. Newton, C.R., Crawley, J., Sowumni, A., Waruiru, C., Mwangi, I., English, M., Murphy, S., Winstanley, P.A., Marsh, K., and Kirkham, F.J. (1997). Intracranial hypertension in Africans with cerebral malaria. Arch. Dis. Child. *76*, 219–226.
44. Bolte, A.C., Dutta, A.B., Hurt, M.E., Smirnov, I., Kovacs, M.A., McKee, C.A., Ennerfelt, H.E., Shapiro, D., Nguyen, B.H., Frost, E.L., et al. (2020). Meningeal lymphatic dysfunction exacerbates traumatic brain injury pathogenesis. Nat. Commun. *11*, 4524.
45. Xiang, T., Feng, D., Zhang, X., Chen, Y., Wang, H., Liu, X., Gong, Z., Yuan, J., Liu, M., Sha, Z., et al. (2022). Effects of increased intracranial pressure on cerebrospinal fluid influx, cerebral vascular hemodynamic indexes, and cerebrospinal fluid lymphatic efflux. J Cereb Blood Flow Metab *42*, 2287–2302.
46. Carare, R.O., Bernardes-Silva, M., Newman, T.A., Page, A.M., Nicoll, J.A.R., Perry, V.H., and Weller, R.O. (2008). Solutes, but not cells, drain from the brain parenchyma along basement membranes of capillaries and arteries: significance for cerebral amyloid angiopathy and neuroimmunology. Neuropathol. Appl. Neurobiol. *34*, 131–144.
47. Hladky, S.B., and Barrand, M.A. (2018). Elimination of substances from the brain parenchyma: efflux via perivascular pathways and via the blood-brain barrier. Fluids Barriers CNS *15*, 30.
48. Bakker, E.N.T.P., Bacskai, B.J., Arbel-Ornath, M., Aldea, R., Bedussi, B., Morris, A.W.J., Weller, R.O., and Carare, R.O. (2016). Lymphatic Clearance of the Brain: Perivascular, Paravascular and Significance for Neurodegenerative Diseases. Cell. Mol. Neurobiol. *36*, 181–194.
49. Johnston, M., Zakharov, A., Papaiconomou, C., Salmasi, G., and Armstrong, D. (2004). Evidence of connections between cerebrospinal fluid and nasal lymphatic vessels in humans, non-human primates and other mammalian species. Cerebrospinal Fluid Res. *1*, 2.
50. Mollanji, R., Bozanovic-Sosic, R., Zakharov, A., Makarian, L., and Johnston, M.G. (2002). Blocking cerebrospinal fluid absorption through the cribriform plate increases resting intracranial pressure. Am. J. Physiol. Regul. Integr. Comp. Physiol. *282*, R1593–R1599.
51. Sokolowski, W., Barszcz, K., Kupczynska, M., Czubaj, N., Skibniewski, M., and Purzyc, H. (2018). Lymphatic drainage of cerebrospinal fluid in mammals - are arachnoid granulations the main route of cerebrospinal fluid outflow? Biologia (Bratisl) *73*, 563–568.
52. Da Mesquita, S., Louveau, A., Vaccari, A., Smirnov, I., Cornelison, R.C., Kingsmore, K.M., Contarino, C., Onengut-Gumuscu, S., Farber, E., Raper, D., et al. (2018). Functional aspects of meningeal lymphatics in ageing and Alzheimer's disease. Nature *560*, 185–191.
53. Moxon, C.A., Chisala, N.V., Wassmer, S.C., Taylor, T.E., Seydel, K.B., Molyneux, M.E., Faragher, B., Kennedy, N., Toh, C.H., Craig, A.G., and Heyderman, R.S. (2014). Persistent endothelial activation and inflammation after Plasmodium falciparum Infection in Malawian children. J. Infect. Dis. *209*, 610–615.
54. Hablitz, L.M., and Nedergaard, M. (2021). The Glymphatic System: A Novel Component of Fundamental Neurobiology. J. Neurosci. *41*, 7698–7711.
55. Goodman, J.R., and Iliff, J.J. (2020). Vasomotor influences on glymphatic-lymphatic coupling and solute trafficking in the central nervous system. J. Cereb. Blood Flow Metab. *40*, 1724–1734.
56. Iliff, J.J., Wang, M., Zeppenfeld, D.M., Venkataraman, A., Plog, B.A., Liao, Y., Deane, R., and Nedergaard, M. (2013). Cerebral arterial pulsation drives paravascular CSF-interstitial fluid exchange in the murine brain. J. Neurosci. *33*, 18190–18199.
57. Ma, Q., Ries, M., Decker, Y., Müller, A., Riner, C., Bücker, A., Fassbender, K., Detmar, M., and Proulx, S.T. (2019). Rapid lymphatic efflux limits cerebrospinal fluid flow to the brain. Acta Neuropathol. *137*, 151–165.
58. Blaumanis, O.R., Rennels, M.L., and Grady, P.A. (1990). Focal cerebral edema impedes convective fluid/tracer movement through paravascular pathways in cat brain. Adv. Neurol. *52*, 385–389.
59. Liu, K., Zhu, J., Chang, Y., Lin, Z., Shi, Z., Li, X., Chen, X., Lin, C., Pan, S., and Huang, K. (2021). Attenuation of cerebral edema facilitates recovery of glymphatic system function after status epilepticus. JCI Insight *6*, e151835.
60. Da Mesquita, S., Papadopoulos, Z., Dykstra, T., Brase, L., Farias, F.G., Wall, M., Jiang, H., Kodira, C.D., de Lima, K.A., Herz, J., et al. (2021). Meningeal lymphatics affect microglia responses and anti-Abeta immunotherapy. Nature *593*, 255–260.
61. Cserr, H.F., Cooper, D.N., Suri, P.K., and Patlak, C.S. (1981). Efflux of radiolabeled polyethylene glycols and albumin from rat brain. Am. J. Physiol. *240*, F319–F328.

62. Reulen, H.J., Tsuyumu, M., Tack, A., Fenske, A.R., and Prioleau, G.R. (1978). Clearance of edema fluid into cerebrospinal fluid. A mechanism for resolution of vasogenic brain edema. J. Neurosurg. *48*, 754–764.

63. Marmarou, A., Hochwald, G., Nakamura, T., Tanaka, K., Weaver, J., and Dunbar, J. (1994). Brain edema resolution by CSF pathways and brain vasculature in cats. Am. J. Physiol. *267* (*2 Pt 2*), H514–H520.

64. Geer, C.P., and Grossman, S.A. (1997). Interstitial fluid flow along white matter tracts: a potentially important mechanism for the dissemination of primary brain tumors. J. Neuro Oncol. *32*, 193–201.

65. Boulton, M., Armstrong, D., Flessner, M., Hay, J., Szalai, J.P., and Johnston, M. (1998). Raised intracranial pressure increases CSF drainage through arachnoid villi and extracranial lymphatics. Am. J. Physiol. *275*, R889–R896.

66. Belov, V., Appleton, J., Levin, S., Giffenig, P., Durcanova, B., and Papisov, M. (2021). Large-Volume Intrathecal Administrations: Impact on CSF Pressure and Safety Implications. Front. Neurosci. *15*, 604197.

67. Wrba, E., Nehring, V., Baethmann, A., Reulen, H.J., and Uhl, E. (1998). Resolution of experimental vasogenic brain edema at different intracranial pressures. Acta Neurochir. Suppl. *71*, 313–315.

68. Louveau, A., Herz, J., Alme, M.N., Salvador, A.F., Dong, M.Q., Viar, K.E., Herod, S.G., Knopp, J., Setliff, J.C., Lupi, A.L., et al. (2018). CNS lymphatic drainage and neuroinflammation are regulated by meningeal lymphatic vasculature. Nat. Neurosci. *21*, 1380–1391.

69. Jafarnejad, M., Woodruff, M.C., Zawieja, D.C., Carroll, M.C., and Moore, J.E., Jr. (2015). Modeling Lymph Flow and Fluid Exchange with Blood Vessels in Lymph Nodes. Lymphat. Res. Biol. *13*, 234–247.

70. Clement, C.C., Wang, W., Dzieciatkowska, M., Cortese, M., Hansen, K.C., Becerra, A., Thangaswamy, S., Nizamutdinova, I., Moon, J.Y., Stern, L.J., et al. (2018). Quantitative Profiling of the Lymph Node Clearance Capacity. Sci. Rep. *8*, 11253.

71. Acton, S.E., Onder, L., Novkovic, M., Martinez, V.G., and Ludewig, B. (2021). Communication, construction, and fluid control: lymphoid organ fibroblastic reticular cell and conduit networks. Trends Immunol. *42*, 782–794.

72. Zakharov, A., Papaiconomou, C., Koh, L., Djenic, J., Bozanovic-Sosic, R., and Johnston, M. (2004). Integrating the roles of extracranial lymphatics and intracranial veins in cerebrospinal fluid absorption in sheep. Microvasc. Res. *67*, 96–104.

73. Bothwell, S.W., Omileke, D., Hood, R.J., Pepperall, D.G., Azarpeykan, S., Patabendige, A., and Spratt, N.J. (2021). Altered Cerebrospinal Fluid Clearance and Increased Intracranial Pressure in Rats 18 h After Experimental Cortical Ischaemia. Front. Mol. Neurosci. *14*, 712779.

74. Kida, S., Pantazis, A., and Weller, R.O. (1993). CSF drains directly from the subarachnoid space into nasal lymphatics in the rat. Anatomy, histology and immunological significance. Neuropathol. Appl. Neurobiol. *19*, 480–488.

75. Ampawong, S., Chaisri, U., Viriyavejakul, P., Nontprasert, A., Grau, G.E., and Pongponratn, E. (2014). Electron microscopic features of brain edema in rodent cerebral malaria in relation to glial fibrillary acidic protein expression. Int. J. Clin. Exp. Pathol. *7*, 2056–2067.

76. Lackner, P., Beer, R., Helbok, R., Broessner, G., Engelhardt, K., Brenneis, C., Schmutzhard, E., and Pfaller, K. (2006). Scanning electron microscopy of the neuropathology of murine cerebral malaria. Malar. J. *5*, 116.

77. Medana, I.M., and Turner, G.D.H. (2006). Human cerebral malaria and the blood-brain barrier. Int. J. Parasitol. *36*, 555–568.

78. Mestre, H., Tithof, J., Du, T., Song, W., Peng, W., Sweeney, A.M., Olveda, G., Thomas, J.H., Nedergaard, M., and Kelley, D.H. (2018). Flow of cerebrospinal fluid is driven by arterial pulsations and is reduced in hypertension. Nat. Commun. *9*, 4878.

79. Berg, S., Kutra, D., Kroeger, T., Straehle, C.N., Kausler, B.X., Haubold, C., Schiegg, M., Ales, J., Beier, T., Rudy, M., et al. (2019). ilastik: interactive machine learning for (bio)image analysis. Nat. Methods *16*, 1226–1232.

80. Lin, J.W., Annoura, T., Sajid, M., Chevalley-Maurel, S., Ramesar, J., Klop, O., Franke-Fayard, B.M.D., Janse, C.J., and Khan, S.M. (2011). A novel 'gene insertion/marker out' (GIMO) method for transgene expression and gene complementation in rodent malaria parasites. PLoS One *6*, e29289.

81. Carroll, R.W., Wainwright, M.S., Kim, K.Y., Kidambi, T., Gómez, N.D., Taylor, T., and Haldar, K. (2010). A rapid murine coma and behavior scale for quantitative assessment of murine cerebral malaria. PLoS One *5*, e13124.

82. Louveau, A., Filiano, A.J., and Kipnis, J. (2018). Meningeal whole mount preparation and characterization of neural cells by flow cytometry. Curr. Protoc. Immunol. *121*, e50.

83. Keep, R.F., Hua, Y., and Xi, G. (2012). Brain water content. A misunderstood measurement? Transl. Stroke Res. *3*, 263–265.

84. Xavier, A.L.R., Hauglund, N.L., von Holstein-Rathlou, S., Li, Q., Sanggaard, S., Lou, N., Lundgaard, I., and Nedergaard, M. (2018). Cannula Implantation into the Cisterna Magna of Rodents. J. Vis. Exp. *135*, 57378.

85. Hablitz, L.M., Vinitsky, H.S., Sun, Q., Stæger, F.F., Sigurdsson, B., Mortensen, K.N., Lilius, T.O., and Nedergaard, M. (2019). Increased glymphatic influx is correlated with high EEG delta power and low heart rate in mice under anesthesia. Sci. Adv. *5*, eaav5447.

86. Pla, V., Bork, P., Harnpramukkul, A., Olveda, G., Ladron-de-Guevara, A., Giannetto, M.J., Hussain, R., Wang, W., Kelley, D.H., Hablitz, L.M., and Nedergaard, M. (2022). A real-time in vivo clearance assay for quantification of glymphatic efflux. Cell Rep. *40*, 111320.

87. Zhang, M., Jasim, D.A., Ménard-Moyon, C., Nunes, A., Iijima, S., Bianco, A., Yudasaka, M., and Kostarelos, K. (2016). Radiolabeling, whole-body single photon emission computed tomography/computed tomography imaging, and pharmacokinetics of carbon nanohorns in mice. Int. J. Nanomedicine *11*, 3317–3330.

88. Simon, M., Wang, M.X., Ismail, O., Braun, M., Schindler, A.G., Reemmer, J., Wang, Z., Haveliwala, M.A., O'Boyle, R.P., Han, W.Y., et al. (2022). Loss of perivascular aquaporin-4 localization impairs glymphatic exchange and promotes amyloid beta plaque formation in mice. Alzheimer's Res. Ther. *14*, 59.

STAR★METHODS

KEY RESOURCES TABLE

REAGENT or RESOURCE	SOURCE	IDENTIFIER
Antibodies		
ICAM-1 (polyclonal)	R&D	Cat#: AF796; RRID:AB_2248703
CD31-PE (clone: 390)	BioLegend	Cat#: 102407; RRID:AB_312902
Smooth muscle actin (polyclonal)	Abcam	Cat#: ab5694; RRID:AB_2223021
Glial fibrillary acidic protein (clone: G-A-5)	Sigma	Cat#: G3893; RRID:AB_477010
Lyve1 (polyclonal)	Abcam	Cat#: ab14917; RRID:AB_301509
CD45 (clone: IBL-3/16)	Bio-Rad	Cat#: MCA1388; RRID:AB_321729
AQP4 (polyclonal)	Millipore	Cat#: ABB2218; RRID:AB_11210366
Chemicals, peptides, and recombinant proteins		
FITC-Albumin	Sigma	Cat#: A9771
Ovalbumin, Alexa Fluor 647 Conjugate	ThermoFisher	Cat#: O34784
Alexa Fluor 594 Hydrazide	ThermoFisher	Cat#: A10438
Artificial Cerebrospinal Fluid	Tocris Bioscience	Cat#: 3525
Biotinylated lectin	Sigma	Cat#: L0651
Experimental models: Organisms/strains		
C57BL/6J mice	Charles River (UK)	RRID:IMSR_JAX:000664
Plasmodium berghei ANKA	Leiden Malaria Research Group	RRID:NCBITaxon_5823
Software and algorithms		
LAS AF v3.1.0.8587	Leica	Leica
Fiji ImageJ (v2.15.1)	Fiji	https://imagej.net/software/fiji/
MoorLAB (v1.0	Moor Instruments	Moor Instruments
Nucline (Build 020.0000)	Mediso	Mediso
VivoQuant (v4.0)	Invicro	Invicro
Fusion (v2.0)	Oxford Instruments	Oxford Instruments
GraphPad Prism 10 (v10.0.2)	GraphPad	GraphPad
SciPy (v1.9.1)	SciPy Foundation	https://scipy.org/about/
Ilastik (v1.3.3)	Berg et al.[79]	https://www.ilastik.org/
devbio-napari (v0.10.1)	Napari	https://github.com/haesleinhuepf/devbio-napari
QuPath (v0.4.4)	QuPath	https://qupath.github.io/

RESOURCE AVAILABILITY

Lead contact

Further information and requests for resources and reagents should be directed to and will be fulfilled by the lead contact, Kevin Couper (kevin.couper@manchester.ac.uk).

Materials availability

This study did not generate new unique reagents.

Data and code availability

- All data reported in this paper will be shared by the lead contact upon request.
- This paper does not report original code.
- Any additional information required to reanalyze the data reported in this work paper is available from the lead contact upon request.

EXPERIMENTAL MODEL AND STUDY PARTICIPANT DETAILS

Female C57BL/6J mice (8–10 week old) were purchased from Charles River (UK) (RRID:IMSR_JAX:000664). All mice were housed in groups of 5 in individually ventilated cages and were randomly assigned to experimental groups. All animal work was approved following local ethical review by the University of Manchester Animal Procedures and Ethics Committees and was performed in accordance with the U. K Home Office Animals (Scientific Procedures) Act 1986 (approved H.O. Project License P8829D3B4).

METHOD DETAILS

Plasmodium berghei ANKA infection and tissue preparation

Cryopreserved *Plasmodium berghei* (Pb) ANKA parasites[80] were thawed and passaged once through C57BL/6 mice before being used to infect experimental animals via intravenous (i.v.) injection of $1x10^4$ pRBCs. Peripheral parasite burden was quantified by microscopic examination of giemsa-stained thin blood smears. The development and recovery from ECM was monitored using the RMCBS,[81] a neurological scoring system for ECM disease severity. Once mice developed early signs of RMCBS (score 11–12 on RMCBS, unless otherwise specified), they were treated with artesunate (i.p. injection of 30 mg/kg, Sigma) in sterile PBS. At the end of most experiments, mice were culled by transcardial perfusion with 4% paraformaldehyde under terminal anesthesia with isoflurane. For assessment of perivascular spaces in H&E sections, post-fixed brains then underwent processing (dehydration through alcohols and xylene) and were embedded in paraffin wax. In specific experiments to measure brain water content, mice were culled by rising concentration of CO_2 and brains and tissues were removed without perfusion (to avoid perturbing fluid balance within the brain). In experiments where radionuclides were administered, animals were culled at the end of the experiment by exsanguination under terminal anesthesia with isoflurane. Fixed tissues (e.g., brain, skull base, skull cap) were dissected and kept at 4°C prior to stereomicroscopy. Meninges were collected in some mice, as previously described,[82] and used for whole-mount microscopy. Brains were then post-fixed in 4% PFA for 24 h, cryoprotected with 20% sucrose, and stored at −20°C.

Assessing brain water content

To assess brain water content, freshly dissected brains were weighed before being dehydrated in an oven for 48 h at 90°C. Brain water content was then calculated as (wet weight - dry weight) ÷ dry weight.[83]

Administration of FITC-albumin to visualise blood-brain barrier breakdown

Animals were injected i.v. with 100 μL of 20 mg/mL FITC-albumin (Sigma-Aldrich, UK) reconstituted in sterile PBS. The tracer was allowed to circulate for 30 min prior to brains being removed and processed, as described above.

Administration of tracers via cisterna magna injection

Administration of tracers via the cisterna magna was conducted as previously published.[21,78,84] Mice were anesthetised using ketamine (70 mg/kg) and xylazine (10 mg/kg), which has been validated as the optimal anesthesia regimen for studying CSF flow within the glymphatic pathway.[85] Surgical areas prepared with shaving, and with the application of betadine and a topical anesthetic (5% EMLA cream). Mice were then secured in a stereotaxic frame at a downward angle of 45°. A midline skin incision was made at the base of the skull, and the fascia dissected to expose the dura mater overlying the cisterna magna. A 30G needle (attached to an injection line and microinjector syringe driver) was used to puncture the cisterna centrally at a 45° angle to the mouse head so that 1–2 mm of the bevel was under the dura. Once in position, the needle was secured in place with cyanoacrylate glue. Mice were then removed from the stereotaxic frame and placed to rest in a natural posture as 10 μL of A647-Ovalbumin tracer (ThermoFisher, dissolved 1% w/v in artificial CSF, Tocris Bioscience) was injected into the cisterna magna over 10 min at 1 μL/min. Following injection, mice were maintained under anesthesia for 30 min before termination. Mice in which tracer administration was incomplete or leakage was observed were excluded from analysis. Body temperature was maintained throughout surgery at 37°C using a homeothermic blanket, and animals recovered from surgery in a heated cabinet (30°C). As intracranial (intraparenchymal) injections can inhibit CSF flow into the brain,[38,86] we did not perform intra cisterna magna and intracranial injections in the same mice.

Administration of tracers via intracerebral injection

Intracerebral tracer injections were conducted using a published method,[52] optimised for quantitatively and accurately assessing the rate of solute efflux from the brain parenchyma.[55] Mice undergoing intracerebral injections were placed under isoflurane anesthesia (2% in 200 mL/min O_2 and 500 mL/min N_2O) for the surgical procedure (approximately 15 min), before being allowed to recover for the remainder of the specified time period prior to termination. Surgical areas prepared with shaving, and with the application of betadine and a topical anesthetic (5% EMLA cream). Mice were then secured in a stereotaxic frame in a horizontal angle. A small midline skin incision was made across the top of the head to expose the skull and, using a cotton bud, the skull membrane was dried. A hole in the skull was drilled at 1.5 mm in the anterior–posterior axis and −1.5 mm in the medial–lateral axis relative to bregma, and a 30G needle was inserted at a depth of 2.5 mm relative to bregma, which was left *in situ* for 5 min to allow the needle tract to swell shut to prevent tracer reflux. 1ul of fluorescent (0.5% A647-ovalbumin and 0.5% A594-hydrazide (Thermofisher) dissolved w/v in artificial CSF [Tocris Bioscience]) or radiotracers (see SPECT/CT section below) was then injected over 5 min using a microinjector. The needle was then

left *in situ* for 5 min to prevent backflow, before being slowly withdrawn, and the injection site sealed with cyanoacrylate glue. The mice were removed from the stereotaxic frame, the scalp skin was sutured, and mice recovered for 1 or 3 (fluorescence) or 4 (radiotracers) hours prior to culling. Mice in which tracer administration was incomplete or leakage was observed were excluded from analysis. There was no evidence of accidental ventricular infusion of tracers in any of our experiments. Body temperature was maintained throughout surgery at 37°C using a homeothermic blanket, and animals recovered from surgery in a heated cabinet (30°C).

Stereomicroscopy

Stereomicroscopy images were collected on a Leica M205 FA upright Stereomicroscope using a DFC 565FX camera (Leica) through LAS AF v3.1.0.8587 software (Leica). Images were processed and analyzed using Fiji ImageJ.

Laser speckle

Mice were anesthetized using isoflurane anesthesia (2% in 200 mL/min O_2 and 500 mL/min N_2O), and secured in a stereotaxic frame (World Precision Instruments, USA) positioned under a Moor FLPI2 Full-Field Perfusion Imager (Moor instruments, UK). The scalp was dissected along the midline, and the skin retracted using surgical clips to expose the skull. An ultrasound gel was then applied to the skull and covered with a glass coverslip. Imaging was performed at 1-min intervals for 5 min with 20 ms exposure time and a 25-frame filter. Analysis was performed over a region of interest drawn over the entire cortical surface using MoorLAB (Moor instruments, UK).

Ligation of afferent lymphatic vessels draining to dcLNs

The afferent vessels supplying the dcLNs were ligated using a published method.[52] Mice were anesthetized with isoflurane, the neck was shaved and cleaned with betadine, and local analgesia applied (5% EMLA cream). A midline incision was then made 5 mm superior to the clavicle, and the sternocleidomastoid muscle was retracted and the dCLN exposed. The afferent vessels that supply the dcLN with lymph from the head and neck were then ligated with 10-0 synthetic, non-absorbable suture. The wound was then sutured closed, cleaned with betidine and local analgesia re-applied (5% EMLA cream). Sterile saline (0.5mL) and buprenorphine (0.05 mg/kg) were administered subcutaneously and mice allowed to recover in heated cabinets before being returned to home cages to recover for 5–7 days prior to infection or further experiments.

Single-Photon emission computerised tomography (SPECT)/CT

Indium chloride ($^{111}InCl_3$) (Curium Pharma, UK) 80 MBq in an ammonium acetate buffer at pH 5.5 was chelated with 10 μL diethylenetriamine pentaacetate (DTPA, Sigma Aldrich (UK), 1 mg/ml prepared.[87] Mice were anesthetized using isoflurane anesthesia (2% in 200 mL/min O_2 and 500 mL/min N_2O) and underwent intracerebral injection with 1 μL of ^{111}In-DTPA (molecular weight 542 Da), with each mouse receiving a dose of ~0.5 MBq. At 30 min and 4 h post-injection, mice were imaged using an SPECT/CT scanner (NanoScan Mediso, Hungary), and animals were allowed to recover from anesthesia between imaging sessions. SPECT images were obtained in 20 projections over 20–30 min using a four-head scanner with 1.4 mm pinhole collimators. X-ray CT scans were taken before each SPECT acquisition using a semi-circular method with full scan, 480 projections, maximum FOV, 35kV energy, 300ms exposure time and 1–4 binning. Acquisitions were done using the Nucline v2.01 (Build 020.0000) software (Mediso, Hungary), while reconstruction of all images and fusion of SPECT with CT images were performed using the Interview Fusion bulletin software (Mediso, Hungary). The images were further analyzed using VivoQuant 4.0 software (Boston, MA, USA). Midpoint images for the different view planes of each time point were chosen by using the middle CT slice of all CT slices displaying tissue from the subject. After the 4-h scan, mice were sacrificed and tissues were harvested. Radioactivity due to ^{111}In decay in tissues was quantified on a gamma counter (PerkinElmer Inc.) alongside a sample of the injected dose for decay correction and calculations of % of injected dose (%ID).

Immunohistochemistry and image analysis

Brains were sectioned either at 30 or 100 μm on a freezing sledge microtome (Bright, UK) or vibratome (Leica VT1000 S), respectively. Whole-mount meninges were detached from skull caps under a dissecting microscope.[82] Decalcified skulls were sectioned at 20 μm on a cryostat as described below. Sections were washed twice with PBS, then incubated with blocking solution (1% BSA, 0.05% Tween 20 in PBS) for 1 h. Blocking solution was then removed, and sections incubated overnight at 4°C with primary antibodies diluted in fresh blocking solution. The tissues (free-floating brain sections, meninges, or decalcified skull sections) were immunostained with biotinylated lectin (10 μg/mL, Sigma, L0651) and/or primary anti-mouse antibodies against the following targets: ICAM-1 (1:250, R&D, polyclonal, AF796), CD31-PE (1:100, BioLegend, 390), smooth muscle actin (SMA, 1:500, Abcam, polyclonal, ab5694), glial fibrillary acidic protein (GFAP) (1:250, Sigma Aldrich, G-A-5), Lyve1 (1:200, Abcam, polyclonal, ab5694), AQP4 (1:250, Millipore, polyclonal, ABB214), CD45 (1:100, Bio-Rad, IBL-3/16, MCA1388). Sections were then washed twice with PBS with 0.05% Tween 20, followed by incubation with anti-IgG Alexa-fluor (ThermoFisher) or biotinylated (Vector) secondary antibodies (1:500 in blocking solution) for 2 h. For confocal assessment of SMA staining, a streptavidin-conjugated Brilliant Violet 421 (BioLegend) fluorophore was used. When necessary, a SuperBoost Alexa 350 Tyramide amplification kit (ThermoFisher) was used, as per manufacturer's instructions. Sections were washed in PBS, mounted from water onto gelatin-coated slides, and covered-slipped with ProLong Gold (Invitrogen).

Images for H&E staining, FITC-albumin, ICAM1, IgG, whole-mount meninges, and tracers (A594-Hydrazide and A647-Ovalbumin) were captured using an Olympus BX63 upright microscope through CellSens Dimension v1 IBL-3/16.16 (Olympus). Analysis of wide-field microscopy images was performed using Fiji ImageJ. Microscopic regions of FITC leakage into the parenchyma ($FITC^+$ foci) were distinguished from regions of low or no FITC leakage ($FITC^-$) by thresholding in Fiji ImageJ on 8 fields of view (10x objective) in the cortex, per mouse. The vessel types present within $FITC^+$ foci were then quantified, with capillaries identifiable by their small diameter, veins identifiable by their diameter, and arteries identifiable by their diameter and presence of SMA staining. Intensity of A647-ovalbumin, FITC, IgG and ICAM-1 staining were quantified as the average fluorescence intensity over the entirety of 8 coronal sections spaced throughout the brain.

Images of AQP4 and for assessment of size of perivascular space, images were captured using an Andor Dragonfly200 spinning disk upright confocal microscope (with a Leica DM6 FS microscope frame). Images were collected using a Zyla 4.2 Plus sCMOS camera and maximal intensity projections presented, and were deconvoluted and analyzed using the Fusion software (Oxford Instruments). For 3D figures, sequences of images were acquired using a Z step size of 100 μm. To analyze the length and fluorescent data for each channel, a line was draw in the area of interest and the data was exported and analyzed using GraphPad PRISM 10 software (GraphPad Software) and the Scipy (v1.9.1) package in Python. In this analysis we hypothesised that intact AQP4 polarisation would be associated with a sharp peak of AQP4 expression associated with a well-defined astrocyte endfoot monolayer, whereas a loss of polarisation would be associated with a more uneven distribution with several peaks as AQP4 expression relocates way from the endfeet toward the astrocyte soma.[88] We therefore compared the perivascular distribution of AQP4 expression to a modeled version in which the AQP4 was in one peak (a Gaussian distribution), corresponding to the endfoot process. Vessels in which the AQP4 staining followed a Gaussian distribution were determined to have good fit to the model, and therefore had intact AQP4 polarisation. Images acquired using Fusion software (Oxford Instruments) were analyzed using IMARIS software (Oxford Instruments) to generate 2D and 3D images.

The area of perivascular space was calculated on H&E sections cut from paraffin blocks on a microtome at 5 μm thickness. Areas of perivascular space were manually annotated on H&E sections in Ilastik (v1.3.3)[79] to train pixel- and object-classifiers, allowing areas of perivascular space to be differentiated from vascular lumen or more general tissue edema. Quantification was performed on 6 fields of view (each 0.7 mm^2) in the cortex.

In whole-mount meninges, the average diameter of lymphatic vessels at the sagittal sinus was calculated from measurements at 15 locations per animal. The number of $CD45^+$ cells in the meninges overlying the cortical surface was quantified using QuPath (v0.4.4).

Images of the vascular localisation of intracerebrally injected tracers (Figure 4) were collected on a Leica SP8x AOBS Inverted confocal using a 20x/0.75 Plan Apo objective. An entire hemisphere of a 100 μm thick coronal section was imaged in 10 z stack positions for each animal, with maximum intensity projections shown. Images were collected using hybrid detectors with channels collected sequentially to prevent crosstalk. Image analysis was performed using devbio-napari (v0.10.1) in Python. A vascular mask was created from the FITC-lectin staining, with arterial portions of the vascular tree identified by reviewing Z-stacks and manually annotating vessels with smooth muscle actin staining. Capillaries and veins were then differentiated based upon average vessel diameter estimated along the skeletons of the vascular structures. The masks of individual vessels were used to calculate the mean intensity of each tracer associated with the vessel. To assess the impact of distance from the injection site on vascular staining, brains were divided into annuli of 250 μm diameter centered on the injection site. In total 52298 vessels were analyzed in 14 animals, including 52298 capillaries, 6633 veins and 969 arteries.

Decalcification of skulls

For tissue decalcification, animals were perfusion-fixed with 4% PFA, and skulls post-fixed for 24h in 4% PFA, then decalcified for 48h in 4% formic acid.[26] For localisation of tracers by stereomicroscopy, skulls were divided down the midline for imaging. For immunohistochemistry, decalcified skulls were then cryoprotected in 20% sucrose, frozen and sectioned on a cryostat at 20 μm thickness.

QUANTIFICATION AND STATISTICAL ANALYSIS

Statistical details of experiments (*n* numbers, statistical tests, *p* value thresholds) can be found in figure legends or panels. Data is presented as mean ± standard error of mean. All statistical analyses were performed using GraphPad PRISM 10 (GraphPad Software) and are detailed alongside relevant *n* numbers in figure legends. Normality was assessed with Shapiro-Wilk tests, and equal variances with Brown–Forsythe tests. Transformations and/or corrections were then applied where necessary.